ELECTROSEISMIC WAVES FROM POINT SOURCES IN LAYERED MEDIA

Matthijs W. Haartsen and M. N. Toksöz

Earth Resources Laboratory
Department of Earth, Atmospheric, and Planetary Sciences
Massachusetts Institute of Technology
Cambridge, MA 02139

ABSTRACT

The macroscopic governing equations controlling the coupled electromagnetics and acoustics of porous media are numerically solved for the case of a layered poro-elastic medium. It is shown that these coupled equations decouple into two equation sets describing two uncoupled wavefield pictures. That is, the $PSVTM$ picture where the compressional and vertical polarized mechanical waves drive currents in the PSV particle motion plane that couples to the electromagnetic wavefield components of the TM mode. And the $SHTE$ picture where the horizontal polarized rotational mechanical waves drive currents in the SH particle motion plane that couples to the electromagnetic wavefield components of the TE mode. The global matrix method is employed in computing electroseismograms in layered poro-elastic media in the $PSVTM$ picture.

The principal features of the converted electromagnetic signals are the following: (1) contacts all antennas at approximately the same time; (2) arrives at the antennas at half of the seismic traveltime at normal incidence reflected P waves; and (3) changes sign on opposite sides of the shot.

The seismic pulse is shown to induce electric fields that travel with the compressional wavespeed and magnetic fields that travel with the rotational wavefield. The frequency content of the converted electromagnetic field has the same frequency content of the driving incident seismic pulse, as long as the propagation distances are much less than the electromagnetic skin depth.

Snapshots in time and converted electromagnetic amplitudes versus seismic point source-antenna offset-are calculated for contrasts in mechanical and/or electrical medium property. Conversion happens there where the seismic wavefront passes a contrast in medium properties due to generated imbalances in current across the contrast. The TM component amplitude radiation pattern away from the interface shows similarities with

an effective electric dipole radiation pattern, or its dual, an effective magnetic current loop radiation pattern centered right beneath the source at the contrast's depth. The TM mode amplitudes decay rapidly with traveled distance and suggest the importance of a Vertical Electroseismic Profiling geometry to enhance recording of the converted electromagnetic signal by positioning the antennas closer to the target (contrast) of interest.

INTRODUCTION

When seismic waves propagate through a fluid saturated sedimentary material, the motion of the pore fluid to the solid matrix causes relative flow. The driving force for the relative flow is a combination of pressure gradients set up by the peaks and throughs of a compressional wave and by grain accelerations. The relative flow caused by grain accelerations can therefore be both due to compressional and shear waves.

A fluid electrolyte in contact with a solid surface chemically absorbs the anions from the electrolyte to the solid wall leaving behind a net excess of cations distributed near the wall. This region is known as an electric double layer (Bockris and Reddy, 1970). The diffuse distribution of mobile cations, with a higher concentration cations in the region close to the absorbed layer and more and more diffuse towards the neutral electrolyte, is free to move when the fluid moves.

The seismic wave motion, which generates the relative flow, also induces a "streaming" electrical current due to the cation motion. This induced streaming current acts as a current source in Maxwell's equations. Therefore, when seismic waves travel through fluid-saturated sedimentary materials, current systems are set up in the material inducing nonradiating fields. But when the seismic waves hit a contrast in electrical and/or mechanical properties, the current systems on both sides form a complex dynamic current system across the interface generating electromagnetic waves.

In this paper, the governing macroscopic equations controlling such behavior will be laid out and these equations will be numerically solved for the case of a layered medium. A global matrix method (Chin *et al.*, 1984; Mal, 1988a,b) is employed in computing the synthetic seismograms in the horizontally stratified medium. The global matrix method solves simultaneously the macroscopic electromagnetic and acoustic-elastic wavefields which drive the current and fluid flow, resulting in a mechanical stress/displacement and electromagnetic wavefield component vector as a function of depth. The equations solved are the coupled poro-elastic (modified Biot's equations) and electromagnetic (Maxwell's) equations. Biot's equations are modified with an induced body force on Biot's equation of relative flow (where the electromagnetic field induces a mechanical force, an osmosis phenomenon). Amperes law in Maxwell's equations has an external current source (where the relative flow has induced an electrical streaming current, an electrokinetic phenomenon). The coupling is given by the transport equations, these flux/force relations relate the current and the relative flow to potential and pressure gradients. The EM field converted from seismic waves traversing boundaries is associated

with a change in the following properties: changes in elastic properties (e.g. porosity, changes in fluid flow permeability, changes in fluid-chemistry that affect the amount of cations free to move in the double layer (e.g., bulk free-ion concentration, pH).

A thick, permeable sand layer example will be presented to show the effect of a mechanical contrast on the mechanical and electromagnetic wavefield components. A fresh water/brine contrast model is used to show the effect of an electrical contrast on the mechanical and electromagnetic wavefield components. Both models are also used in the calculation of converted magnetic and electric field amplitudes versus seismic source-antenna offset at different distances from the interface. Snapshots in time are calculated to follow the conversion evolution of mechanical waves into electromagnetic waves. The rapid decay in amplitude with traveled distance of the converted electromagnetic signal, driven by the seismic source with a seismic center frequency, suggests the Vertical Electroseismic Profiling geometry, where antennas are positioned close to the target of interest. The last two numerical examples are calculations in a VESP geometry.

MACROSCOPIC COUPLED ELECTROMAGNETIC AND PORO-ELASTIC FIELD EQUATIONS

The macroscopic, fully coupled, mechanical, electromagnetic equations and constitutive relations in volume averaged from describing the coupled field behavior in two phase porous medium are (Pride, 1994):

The electromagnetic field equations,

$$\nabla \times \underline{E} = i\omega \underline{B} \tag{1}$$

$$\nabla \times \underline{H} = -i\omega \underline{D} + \underline{J} \tag{2}$$

$$\underline{D} = \epsilon_0 \left[\frac{\phi}{\alpha_\infty} (\kappa_f - \kappa_s) + \kappa_s \right] \underline{E} \tag{3}$$

$$\underline{B} = \mu_0 \underline{H} \tag{4}$$

$$\underline{J} = \sigma(\omega) \underline{E} + L(\omega) \left[-\nabla P + \omega^2 \rho_f \underline{u}_s \right] \tag{5}$$

$$-i\omega \underline{w} = L(\omega) \underline{E} + \frac{k(\omega)}{\eta} \left[-\nabla P + \omega^2 \rho_f \underline{u}_s \right] \tag{6}$$

and the mechanical field equations,

$$\nabla \cdot \underline{\underline{\tau}}_B = -\omega^2 \left[\rho_B \underline{u} + \rho_f \underline{w} \right] \tag{7}$$

$$\underline{\underline{\tau}}_B = \left[K_G \nabla \cdot \underline{u}_s + C \nabla \cdot \underline{w} \right] \underline{\underline{I}} + G_{fr} \left[\nabla \underline{u}_s + \nabla \underline{u}_s^T - \frac{2}{3} \nabla \cdot \underline{u}_s \underline{\underline{I}} \right] \tag{8}$$

$$-P = C\nabla \cdot \underline{u}_s + M\nabla \cdot \underline{w}. \tag{9}$$

Equations (1)– (4) describe the electromagnetic wavefields and equations (7)– (9) the mechanical wavefields. All coupling is present in the transport equations (5)– (6).

The coefficients in the flux equations relating the equations of mass—here fluid flow and current flow when there are potential and pressure gradients—are the frequency dependent conductivity of the two phase medium, $\sigma(\omega)$, the dynamic permeability, $k(\omega)$ and the fluid viscosity, η. The first term in equation (5) is the conduction current contribution, and the second term is the streaming current contribution to the total current. The forces which drive the relative flow are a combination of pressure gradients set up by the peaks and throughs of a compressional wave and by grain acceleration. The relative flow caused by grain acceleration can, therefore, be both due to compressional and shear waves. The fact that the cross terms have the same coupling coefficient $L(\omega)$ is a statement of Onsager reciprocity. The coefficient equality implicates the action of the electric field on the charge density to be reciprocal to the action of the fluid pressure on the charge, or the mobility of the ion is independent of the charge moving through the fluid or of the fluid moving around the charge.

The frequency dependent coefficients are obtained by Pride (1994), where they are explicitly obtained by a volume averaging procedure of Maxwell's equations coupled to Biot's equations. Two possible functions that smoothly connect the low and high frequency regimes of the transport coefficients are,

$$\frac{k(\omega)}{k_0} = \left[\left[1 - i\frac{\omega}{\omega_t}\frac{4}{m}\right]^{1/2} - i\frac{\omega}{\omega_t}\right]^{-1} \tag{10}$$

and,

$$\frac{L(\omega)}{L_0} = \left[1 - i\frac{\omega}{\omega_t}\frac{m}{4\alpha_\infty^2}\left(1 - 2\alpha_\infty\frac{\tilde{d}}{\Lambda}\right)^2\left(1 - i^{3/2}\tilde{d}\sqrt{\frac{\omega\rho_f}{\eta}}\right)^2\right]^{-1/2}. \tag{11}$$

The transition frequency ω_t separates the low frequency viscous flow behavior from the high frequency inertial flow and is defined as,

$$\omega_t = \frac{\phi}{\alpha_\infty k_0}\frac{\eta}{\rho_f} \tag{12}$$

The dimensionless number m is defined as,

$$m \equiv \frac{\phi\Lambda^2}{\alpha_\infty k_0} \tag{13}$$

This number consists only of geometry terms. The low frequency coupling coefficients L_0 is,

$$L_0 = -\frac{\phi}{\alpha_\infty}\frac{\epsilon_0\kappa_f\zeta}{\eta}\left[1 - 2\alpha_\infty\frac{\tilde{d}}{\Lambda}\right]. \tag{14}$$

With κ_f, the relative fluid permittivity, ζ, the zeta potential, and α_∞, the tortuosity (normally a number between 3 and 10). The "$\sqrt{\frac{\omega\rho_f}{\eta}}$" factor in equation (11) determines the viscous skin depth and $\tilde{d} \leq \frac{3\times10^{-10}}{\sqrt{C}} \equiv$ Debye length (which is a measure of the electric double layer thickness) and with C the salinity of the pore fluid. The Λ parameter is the same as defined by Johnson *et al.* (1987). An important factor affecting the electrokinetic coefficient is the ζ-potential. The ζ-potential employed in the numerical calculations is taken from experimental studies. These ζ-potential values are based on saturated NaCl, KCl quartz samples at $T = 25^oC$ and $pH = 7$, determined by Gaudin and Fuerstenau (1955), Sidorova and Fridirkhsberg (1975), and Hidalgo-Alverez and Pardo (1985). Regression analysis applied on their combined data sets resulted in the following ζ-potential as function of electrolyte concentration.

$$\zeta(V) = 0.008 + 0.026 log_{10}(C) \tag{15}$$

The coefficients in the deformation equations are,

$$K_G = H - \frac{4}{3}G = \frac{K_{fr} + \phi K_{fr} + (1-\phi)K_s\Delta}{1+\Delta} \tag{16}$$

$$C = \frac{K_f + K_s\Delta}{1+\Delta} \tag{17}$$

$$M = \frac{1}{\phi}\frac{K_f}{1+\Delta} \tag{18}$$

where the parameter Δ is defined as,

$$\Delta = \frac{K_f}{\phi K_s^2}\left[(1-\phi)K_s - K_{fr}\right]. \tag{19}$$

The moduli K_{fr} and G_{fr} are the bulk and shear moduli of the framework of the grains, when fluid is absent. The frame moduli may either be considered experimentally determined, or may be obtained from approximate theoretical models for specific pore grain geometries. C and M are the incompressibilities used by Biot (1962) and Pride *et al.* (1992), they are complex and frequency dependent, allowing for losses in addition to those associated with relative flow.

TRANSFORM-DOMAIN ELECTROSEISMIC WAVEFIELD CONSTITUENTS IN AN ISOTROPIC PORO-ELASTIC LAYERED MEDIUM

In this section, the compressional (P_f, P_s), rotational (SV, SH) and electromagnetic fields $(TM, TE$ modes) in layered isotropic fully saturated poro-elastic media are investigated. Only mechanical waves are generated by a localized explosive source situated at the interface between two adjacent layers (or subdomains) of the stratified configuration. The seismic wave motion which causes relative flow induces a "streaming"

electrical current due to the excess cation motion, in the electric double layer. The induced streaming current acts as a current source in Amperes current law, equations (2) and (5). Therefore, when seismic waves travel through fluid saturated porous media, current systems are set up. When compressional waves travel through homogeneous porous material, the pressure gradients set up by the peaks and throughs cause the charge to separate (Figure 1). This induces within the seismic pulse a system of electric fields that travel with the compressional wave speed. By symmetry arguments within the seismic pulse (a ricker wavelet in the numerical modeling), there is no net current imbalance and, therefore, the seismic pulse cannot act as an electromagnetic source and radiate electromagnetic waves away from the pulse.

When rotational waves travel through homogeneous porous material, the grain accelerations which are equivoluminal set up current sheets, (Figure 2). This induces within the seismic pulse a magnetic field system that travels with the rotational mechanical wavespeed. By similar symmetry arguments for the induced current sheets within the seismic pulse, the seismic pulse does not radiate electromagnetic fields.

Compressional and vertical polarized rotational mechanical waves can only generate currents in the PSV particle motion plane in homogeneous isotropic poro-elastic media. This couples to the electromagnetic wavefield components of the TM mode. We will call this from now on the $PSVTM$ coupled electroseismic picture. The horizontal polarized rotational mechanical waves can only generate current in the SH particle motion plane in homogeneous isotropic poro-elastic media. This couples to the electromagnetic wavefield components of the TE mode. We will call this from now on the $SHTE$ coupled electroseismic picture.

But when seismic waves hit a contrast in electrical and/or mechanical properties, the current systems within the seismic pulse on both sides become unbalanced and form a complex dynamic current system across the interface generating electromagnetic waves. These EM fields converted from seismic waves traversing boundaries are associated with a change in the following properties: changes in elastic properties (e.g., porosity), changes in fluid flow permeability, and changes in fluid-chemistry that affect the amount of cations free to move in the double layer (e.g., bulk free-ion concentration, pH).

Transform-Domain Field Description

The following geometry description is used: the domain or layer occupied by the mth layer is denoted by D_m, $m = 1, ..., ND$. Each layer is characterized by its (frequency dependent) elastic, electromagnetic properties, and hydraulic and electrical transport properties. The fundamental input properties, used in the numerical modeling, which determine all wavefield velocities, the electrical conductivity, and the electrokinetic coupling coefficients, are: porosity, dc permeability, bulk modulus of the solid and fluid phase, the frame's bulk and shear modulus, the densities of the solid and fluid phase, the viscosity of the fluid phase, the temperature of the bulk material, the tortuosity, the salinity of the fluid, and the relative permittivities of the solid and fluid phases.

First, the transform-domain field equations, describing the wave behavior in each

layer, need to be determined. Next, those field components that are discontinuous across an interface between two media with different poro-elastic and/or electromagnetic properties are eliminated. The resulting differential equations are written in the form of a first-order ordinary matrix differential equation. Since the geometry has azimuthal symmetry, it is natural to use cylindrical coordinates (r, ϕ , z) with z being depth. First, the following definitions involving the horizontal components and horizontal derivatives are employed (e.g., Hudson, 1969; Kennett, 1983),

$$u_V = \frac{1}{r}\left[\frac{\partial}{\partial r}(ru_r) + \frac{\partial}{\partial \phi}u_\phi\right] \tag{20}$$

$$u_H = \frac{1}{r}\left[\frac{\partial}{\partial r}(ru_\phi) - \frac{\partial}{\partial \phi}u_r\right] \tag{21}$$

$$\tau_{Vz} = \frac{1}{r}\left[\frac{\partial}{\partial r}(r\tau_{rz}) + \frac{\partial}{\partial \phi}\tau_{\phi z}\right] \tag{22}$$

$$\tau_{Hz} = \frac{1}{r}\left[\frac{\partial}{\partial r}(r\tau_{\phi z}) - \frac{\partial}{\partial \phi}\tau_{zr}\right] \tag{23}$$

$$< E,H >_V = \frac{1}{r}\left[\frac{\partial}{\partial r}(r < E,H >_r) + \frac{\partial}{\partial \phi} < E,H >_\phi\right] \tag{24}$$

$$< E,H >_H = \frac{1}{r}\left[\frac{\partial}{\partial r}(r < E,H >_\phi) - \frac{\partial}{\partial \phi} < E,H >_r\right] \tag{25}$$

$$\nabla_1^2 = \frac{1}{r}\frac{\partial}{\partial r}\left(r\frac{\partial}{\partial r}\right) + \frac{1}{r^2}\frac{\partial^2}{\partial \phi^2} \tag{26}$$

to rewrite the governing macroscopic, coupled electromagnetic and poro-elastic field equations. It is advantageous to employ the invariance properties of the configuration. The equations are first Fourier transformed to the temporal frequency, where linear time invariance of the system is assumed (note $\frac{\partial}{\partial t} \rightarrow -i\omega$). To take advantage of the shift invariance of the configuration in the horizontal plane, a Finite Fourier Hankel transform is performed over the horizontal coordinates r and ϕ thus providing a cylindrical wave decomposition.

This transform pair is defined as,

$$HF\left[\psi(r,\phi)\right] = \hat{\psi}(k,n) = \frac{1}{2\pi}\int_0^\infty dr r J_n(kr)\int_0^{2\pi} d\phi e^{-in\phi}\psi(r,\phi) \tag{27}$$

$$HF^{-1}\left[\hat{\psi}(k,n)\right] = \psi(r,\phi) = \int_0^\infty dk k \sum_{n=-N}^{N} J_n(kr)e^{in\phi}\hat{\psi}(k,n). \tag{28}$$

Note the property $HF\left[\nabla_1^2\psi\right] = -k^2\hat{\psi}$, (Watson, 1966). The magnitude N in the summation is determined by the azimuthal symmetry of the point source. For spherically symmetric sources there is no azimuthal dependence, then $N = 0$. If the source can be described using an arbitrarily directed force vector, then $N \leq 1$, while if it can be described using a second order moment tensor, then $N \leq 2$ (Kennett, 1983).

The first-order linear matrix differential equation satisfied by $B_J^{(m)}$ is,

$$\frac{\partial}{\partial z}B_I^{(m)} = A_{I,J}^{(m)}B_J^{(m)} + S_I^{(m)} \quad for \quad z_{m-1} < z < z_m, \quad m = 2, ..., ND - 1 \tag{29}$$

$$\frac{\partial}{\partial z}B_I^{(1)} = A_{I,J}^{(1)}B_J^{(1)} \quad for \quad -\infty < z < z_1 \tag{30}$$

$$\frac{\partial}{\partial z}B_I^{(ND)} = A_{I,J}^{(1)}B_J^{(ND)} \quad for \quad z_{ND-1} < z < \infty \tag{31}$$

where the field vector B_J, representative of the transform-domain displacement-stress-EM field components in the subdomain D_m, is denoted by $B_J^{(m)}$ and defined as,

$$B_J^{(m;PSVTM)} = \left[\hat{u}_1, \hat{u}_z, \hat{w}_z, \hat{\tau}_1, \hat{\tau}_{zz}, \hat{T}_p, \hat{H}_2, \hat{E}_1\right]^T \tag{32}$$

$$B_J^{(m;SHTE)} = \left[\hat{u}_2, \hat{\tau}_2, \hat{H}_1, \hat{E}_2\right]^T. \tag{33}$$

These wavefield vector components are just the ones that are continuous across an interface. The field vector components are arrived at by requiring the continuity of the electromagnetic and poro-elastic Poynting vector in the direction perpendicular to the wavefront upon crossing an interface. This also guarantees a consistent macroscopic theory of energy transfer (Haartsen, 1995, chapter 3). The necessary boundary conditions are sufficient for uniqueness of the solution of the macroscopic field equations, as far as this uniqueness is based on energy considerations. Since there are four different up and down going traveling wavetypes in each poro-elastic layer (P_{fast}, P_{slow}, SV and TM) in the $PSVTM$ picture, they impose eight boundary conditions that require continuity of eight wavefield components at both sides of the interface. The $SHTE$ has two up and down traveling wavetypes and, therefore, requires four boundary conditions. The explicit boundary conditions that determine uniquely the displacement-stress-EM field components, (32) and (33), are discussed in Haartsen (1995, chapter 3).

For isotropic media, the first-order ordinary differential equations decompose into two sets that describe the $PSVTM$ picture, the compressional P_{fast} and P_{slow}, vertical polarized shear and TM polarized EM wavefield behavior, and the $SHTE$ picture, the horizontal polarized shear and TE polarized EM wavefield behavior. The first picture describes the changes in z of the field quantities

$$B_J^{(PSVTM)} = \left[\hat{u}_1, \hat{u}_z, \hat{w}_z, \hat{\tau}_1, \hat{\tau}_{zz}, \hat{T}_p, \hat{H}_2, \hat{E}_1\right]^T.$$

The second picture describes the changes in z of the field quantities

$$B_J^{(SHTE)} = \left[\hat{u}_2, \hat{\tau}_2, \hat{H}_1, \hat{E}_2\right]^T.$$

The horizontal components are defined as follows,

$$\hat{u}_1 = \frac{\hat{u}_V}{ik} \qquad \hat{\tau}_1 = \frac{\hat{\tau}_{Vz}}{ik} \qquad \hat{H}_2 = \frac{\hat{H}_H}{ik} \qquad \hat{E}_1 = \frac{\hat{E}_V}{ik} \tag{34}$$

$$\hat{u}_2 = \frac{\hat{u}_H}{ik} \qquad \hat{\tau}_2 = \frac{\hat{\tau}_{Hz}}{ik} \qquad \hat{H}_1 = \frac{\hat{H}_V}{ik} \qquad \hat{E}_2 = \frac{\hat{E}_H}{ik}. \tag{35}$$

If a line source parallel with the stratification is considered instead, then a plane wave decomposition is employed. Working in the (x, y, z) Cartesian coordinates, assuming the line source to be parallel with the y axis, and taking a Fourier transform of the equations of motion with respect to x results in exactly the same equations as are obtained when the following identification of the horizontal components in the displacement-stress-EM vectors are made: $\hat{u}_1 = \hat{u}_x, \hat{u}_2 = \hat{u}_y, \hat{\tau}_1 = \hat{\tau}_{xz}, \hat{\tau}_2 = \hat{\tau}_{yz}, \hat{H}_H = \hat{H}_y, \hat{H}_V = \hat{H}_x, \hat{E}_H = \hat{E}_y, \hat{E}_V = \hat{E}_x$. Thus, using this mapping, it follows that the solution of $\frac{\partial}{\partial z} B_I = A_{IJ} B_J$ applies directly to the line source problem as well. Additionally, the cylindrical wave reflection/transmission coefficients to be obtained are necessarily identical to the plane wave coefficients.

Where $A_{IJ}^{(PSVTM)}$ is a 8 by 8 system matrix, and $S_I^{(PSVTM)}$ is a 8 by 1 notional source matrix, $A_{IJ}^{(SHTE)}$ is a 4 by 4 system matrix, and S_I^{SHTE} a 4 by 1 notional source matrix. The system matrix entries depend on frequency and frequency dependent poro-elastic, electric, and magnetic medium properties and on the horizontal slowness p (note $k = \omega p$). The first-order linear differential matrix equations describing the $PSVTM$ case in the transform domain becomes now,

$$\frac{\partial}{\partial z} B_I^{(PSVTM)} = \begin{bmatrix} -i\omega p \underline{\underline{a}}_{11} & \underline{\underline{a}}_{12} & \underline{\underline{a}}_{13} \\ -\omega^2 \underline{\underline{a}}_{21} & -i\omega p \underline{\underline{a}}_{11}^T & \underline{\underline{a}}_{23} \\ -\omega^2 \underline{\underline{a}}_{31} & -i\omega p \underline{\underline{a}}_{32} & \underline{\underline{a}}_{33} \end{bmatrix} B_J^{(PSVTM)} \tag{36}$$

with, $B_J^{(PSVTM)} = \left[\hat{u}_1, \hat{u}_z, \hat{w}_z, \hat{\tau}_1, \hat{\tau}_{zz}, \hat{T}_p, \hat{H}_2, \hat{E}_1\right]^T$.

With the submatrices given by,

$$\underline{\underline{a}}_{11} = \begin{bmatrix} 0 & 1 & 0 \\ \alpha & 0 & 0 \\ -\beta & 0 & 0 \end{bmatrix}, \quad \underline{\underline{a}}_{12} = \begin{bmatrix} \frac{1}{G} & 0 & 0 \\ 0 & \frac{M}{\Delta} & -\frac{C}{\Delta} \\ 0 & -\frac{C}{\Delta} & \frac{H}{\Delta} - \frac{p^2}{\rho_E} \end{bmatrix}, \quad \underline{\underline{a}}_{13} = \underline{\underline{0}} \tag{37}$$

$$\underline{\underline{a}}_{21} = \begin{bmatrix} B - 2p^2 G(1+\alpha) & 0 & 0 \\ 0 & \rho_B & \rho_f \\ 0 & \rho_f & \rho_E \left(1 + i\omega^3 \frac{\rho_E L^2}{\epsilon}\right) \end{bmatrix}, \quad \underline{\underline{a}}_{23} = \begin{bmatrix} 0 & 0 \\ 0 & 0 \\ -\omega^2 p \frac{\rho_E L}{\epsilon} & 0 \end{bmatrix} \tag{38}$$

$$\underline{\underline{a}}_{31} = \begin{bmatrix} L\rho_f & 0 & 0 \\ 0 & 0 & \frac{L\rho_E}{\epsilon} \end{bmatrix}, \quad \underline{\underline{a}}_{32} = \begin{bmatrix} 0 & 0 & L \\ 0 & 0 & 0 \end{bmatrix}, \quad \underline{\underline{a}}_{33} = \begin{bmatrix} 0 & i\omega\epsilon \\ -\omega\mu\left(i - \frac{p^2}{\mu\epsilon}\right) & 0 \end{bmatrix}. \tag{39}$$

The first order differential matrix equation describing the $SHTE$ case in the transform domain becomes now,

$$\frac{\partial}{\partial z} B_I^{(SHTE)} = \begin{bmatrix} 0 & \frac{1}{G} & 0 & 0 \\ -\omega^2 (\beta - p^2 G) & 0 & 0 & 0 \\ \omega^2 L \rho_f & 0 & 0 & -i\omega\epsilon \left(1 - \frac{p^2}{\mu\epsilon}\right) \\ 0 & 0 & -i\omega\mu & 0 \end{bmatrix} B_J^{(SHTE)} \tag{40}$$

with, $B_J = \left[\hat{u}_2, \hat{\tau}_2, \hat{H}_1, \hat{E}_2\right]^T$. Where the 6 by 6 submatrix, $PSVTM$ picture, and 2 by 2 submatrix, $SHTE$ picture,

$$A_{IJ}^{(Biot;PSVTM)} = \begin{bmatrix} -i\omega p \underline{\underline{a}}_{11} & \underline{\underline{a}}_{12} \\ -\omega^2 \underline{\underline{a}}_{21} & -i\omega p \underline{\underline{a}}_{11}^T \end{bmatrix}, \quad A_{IJ}^{(Biot;SHTE)} = \begin{bmatrix} 0 & \frac{1}{G} \\ -\omega^2 (\beta - p^2 G) & 0 \end{bmatrix} \tag{41}$$

relate the mechanical stress-displacement wavefields with depth.

Where the 2 by 2 submatrix, $PSVTM$ picture, and 2 by 2 submatrix, $SHTE$ picture,

$$A_{IJ}^{(Maxwell;PSVTM)} = \underline{\underline{a}}_{33}, \quad A_{IJ}^{(Maxwell;SHTE)} = \begin{bmatrix} 0 & -i\omega \left(1 - \frac{p^2}{\mu\epsilon}\right) \\ -i\omega\mu & 0 \end{bmatrix} \tag{42}$$

relate the electric and magnetic wavefield components with depth.

Where the 6 by 2 submatrix, $PSVTM$ picture, and 2 by 2 submatrix, $SHTE$ picture,

$$A_{IJ}^{(electrokinetic;PSVTM)} = \begin{bmatrix} -\omega^2 \underline{\underline{a}}_{31} & -i\omega p \underline{\underline{a}}_{32} \end{bmatrix}, \quad A_{IJ}^{(electrokinetic;SHTE)} = \begin{bmatrix} \omega^2 L \rho_f & 0 \\ 0 & 0 \end{bmatrix} \tag{43}$$

relate the electric and magnetic wavefield components, converted from the mechanical wavefields, with depth.

And where the 2 by 6 submatrix, $PSVTM$ picture, and 2 by 2 submatrix, $SHTE$ picture,

$$A_{IJ}^{(osmosis;PSVTM)} = \begin{bmatrix} \underline{\underline{a}}_{13} \\ \underline{\underline{a}}_{23} \end{bmatrix}, \quad A_{IJ}^{(osmosis;SHTE)} = \underline{\underline{0}} \tag{44}$$

relate the mechanical wavefield components, converted from electric and magnetic wavefields, with depth.

The following coefficients have been used in the matrices above.

$$\alpha = 1 - \frac{2GM}{\Delta} \qquad \beta = \frac{\rho_f}{\rho_E} - \frac{2GC}{\Delta} \tag{45}$$

$$\Delta = HM - C^2 \qquad B = \rho_B - \frac{\rho_f^2}{\rho_E} \tag{46}$$

$$\epsilon = \epsilon_0 \kappa(\omega) + i\frac{\sigma(\omega)}{\omega}. \tag{47}$$

Solution Procedure to Obtain Wavefield Constituents

To obtain the wavefields in each layer, the continuity conditions at each boundary are used.

$$\lim_{z\downarrow z_m} B_J^{(m+1)} - \lim_{z\uparrow z_m} B_J^{(m)} = 0 \quad m \neq s \tag{48}$$

At the source level $z = z_s$, where the localized source is situated, B_J jumps by a finite amount. At the source level,

$$\lim_{z\downarrow z_s} B_J^{(s+1)} - \lim_{z\uparrow z_s} B_J^{(s)} = S_J \tag{49}$$

with S_J the source vector. Furthermore, $B_J^{(1)}$ and $B_J^{(ND)}$ must satisfy the radiation conditions,

$$B_J^{(1)} = 0 \qquad z \to -\infty \tag{50}$$

$$B_J^{(ND)} = 0 \qquad z \to \infty. \tag{51}$$

A linear transformation on each of the ND field matrices $B_J^{(m)}$ is carried out. Through it, a field-vector-formalism is obtained in which a decomposition of $B_I^{(m)}$ into up and downgoing fields is manifest. Let $W_N^{(m;PSVTM)}$ be the 8 by 1 matrix and $W_N^{(m;SHTE)}$ the 4 by 1 matrix that is related to $B_J^{(m)}$ by the linear transformation,

$$B_J^{(m)} = D_{J,N}^{(m)} W_N^{(m)} \tag{52}$$

where the composition matrix $D_{J,N}^{(m)}$ is subject to a convenient choice. From the theory of matrices $D_{J,N}^{(m)}$ is taken the eigencolumn matrix of the system matrix $A_{I,J}^{(m)}$

$$\begin{aligned} D_{J,N}^{(m;PSVTM)} &= \Big[b_J^{(m;-P_f)}, b_J^{(m;-P_s)}, b_J^{(m;-SV)}, b_J^{(m;-TM)}, b_J^{(m;+P_f)}, b_J^{(m;+P_s)}, \\ &\qquad b_J^{(m;+SV)}, b_J^{(m;+TM)}\Big] \end{aligned} \tag{53}$$

$$D_{J,N}^{(m;SHTE)} = \Big[b_J^{(m;-SH)}, b_J^{(m;-TE)}, b_J^{(m;+SH)}, b_J^{(m;+TE)}\Big] \tag{54}$$

where $b_J^{(m;\pm r)}$, $r \in P_{fast}, P_{slow}, SV, SH, TM, TE$ denote the eigenvectors of the system matrices $A_{I,J}^{(m)}$. The eigenvectors are derived in Haartsen (1995, chapter 3).

For later convenience the elements of $W_N^{(m)}$ are $W_r^{(m;\pm)}$ with the convention

$$\begin{aligned} W_N^{(m;PSVTM)} &= \Big[W_{P_f}^{(m;-)}, W_{P_s}^{(m;-)}, W_{SV}^{(m;-)}, W_{TM}^{(m;-)}, W_{P_f}^{(m;+)}, W_{P_s}^{(m;+)}, \\ &\qquad W_{SV}^{(m;+)}, W_{TM}^{(m;+)}\Big]^T \end{aligned} \tag{55}$$

$$W_N^{(m;SHTE)} = \left[W_{SH}^{(m;-)}, W_{TE}^{(m;-)}, W_{SH}^{(m;+)}, W_{TE}^{(m;+)}\right]^T. \tag{56}$$

Substituting equation (52) into equation (29) and premultiplication by $D_{M,I}^{(m)-1}$ yields the desired matrix differential equation for $W_N^{(m)}$

$$\frac{\partial}{\partial z} W_M^{(m)} = \Lambda_{M,N}^{(m)} W_N^{(m)} \tag{57}$$

where $\Lambda_{M,N}^{(m)}$ is the diagonal matrix of the eigenvalues $q^{(m;\pm r)}$ of system matrix $A_{I,J}^{(m)}$, and the diagonal matrix $\Lambda_{M,N}$ is defined as,

$$\begin{aligned}\Lambda_{M,N}^{(m;PSVTM)} &= diag\left[q^{(m;-P_f)}, q^{(m;-P_s)}, q^{(m;-SV)}, q^{(m;-TM)}, q^{(m;+P_f)}, q^{(m;+P_s)},\right. \\ &\quad \left. q^{(m;+SV)}, q^{(m;+TM)}\right]\end{aligned} \tag{58}$$

$$\Lambda_{M,N}^{(SHTE)} = diag\left[q^{(m;-SH)}, q^{(m;-TE)}, q^{(m;+SH)}, q^{(m;+TE)}\right]. \tag{59}$$

For each subdomain D_m the system of first-order linear differential equations is now mutually uncoupled. The field matrix $W_N^{(m)}(z)$ of the subdomain D_m is coupled to the field matrix $W_N^{(m+1)}(z)$ of the subdomain D_{m+1} through the boundary conditions, equation (48) at the interface $z = z_m$ between D_m and D_{m+1}.

$$\lim_{z \downarrow z_m} D_{J,N}^{(m+1)} W_N^{(m+1)} - \lim_{z \uparrow z_m} D_{J,N}^{(m)} W_N^{(m)} = 0 \quad m \neq s \tag{60}$$

while at the source level $z = z_s$,

$$\lim_{z \downarrow z_s} D_{J,N}^{(s+1)} W_N^{(s+1)} - \lim_{z \uparrow z_s} D_{J,N}^{(s)} W_N^{(s)} = S_J. \tag{61}$$

Since there are $ND - 1$ interfaces, equations (60) and (61) represent $8 \times (ND$ - 1), the $PSVTM$ picture, or $4 \times (ND$ - 1), the $SHTE$ picture, linear algebraic equations of which the eight or four that follow from equation (61) are inhomogeneous. Next, for each subdomain D_m, the field matrix $W_N^{(m)}(z)$ is written in terms of the linear independent functions $\Gamma^{(m;\pm r)}(z)$ that express the decomposition into up and downgoing fields in D_m.

$$\begin{aligned}\Gamma_{M,K}^{(m;PSVTM)} &= diag\left[\Gamma^{(m;-P_f)}, \Gamma^{(m;-P_s)}, \Gamma^{(m;-SV)}, \Gamma^{(m;-TM)}, \Gamma^{(m;+P_f)}, \Gamma^{(m;+P_s)},\right. \\ &\quad \left. \Gamma^{(m;+SV)}, \Gamma^{(m;+TM)}\right]\end{aligned} \tag{62}$$

$$\Gamma_{M,K}^{(m;SHTE)} = diag\left[\Gamma^{(m;-SH)}, \Gamma^{(m;-TE)}, \Gamma^{(m;+SH)}, \Gamma^{(m;+TE)}\right] \tag{63}$$

where $\Gamma_{M,K}^{(m)}(z)$ are solutions of differential equations (29).

$$\frac{\partial}{\partial z} \Gamma_{M,K}^{(m)} = \Lambda_{M,N}^{(m)} \Gamma_{N,K}^{(m)}. \tag{64}$$

The diagonal elements $\Gamma^{(m;\pm r)}(z)$ of $\Gamma^{(m)}_{M,K}(z)$ are given by,

$$\Gamma^{(m;-r)}(z) = exp[i\omega q^{(m;-r)}(z - z_m)] \quad for \quad z_{m-1} < z < z_m \tag{65}$$

$$\Gamma^{(m;+r)}(z) = exp[-i\omega q^{(m;+r)}(z - z_{m-1})] \quad for \quad z_{m-1} < z < z_m. \tag{66}$$

The source matrix S_I contains a concentrated source and has the form,

$$S_I = \hat{\phi}(\omega) X_I \delta(z - z_s) \tag{67}$$

where $\hat{\phi}(\omega)$ is the Fourier transform of the source signature $\phi(t)$ and X_I is the 8 by 1 or 4 by 1 vector that depends on the nature of the source. Combining equations (57), (60)– (62) and (67) the following expression for $W^{(m)}_N(z)$ is arrived at,

$$W^{(m)}_N(z) = \hat{\phi}(\omega)\Gamma^{(m)}_{N,M}(z)\tilde{W}^{(m)}_M. \tag{68}$$

The coefficient $\tilde{W}^{(m)}_M$ expresses the action of the source as well as the influence of the poro-elastic and electromagnetic properties of each layer. They follow from the boundary conditions at each of the ND-1 interfaces, equations (60) and (61). The transform-domain electromagnetic field matrix $B^{(m)}_J$ of the subdomain D_m is related to $\tilde{W}^{(m)}_M$ via the linear transformation,

$$B^{(m)}_J(k, \omega, z) = \hat{\phi}(\omega) D_{J,N} \Gamma^{(m)}_{N,M}(z)\tilde{W}^{(m)}_M. \tag{69}$$

The righthand side of equation (69) can be recognized as the superposition of eighth (the $PSVTM$ picture), four (the $SHTE$ picture) terms, each corresponding to a transform-domain field component. In the $PSVTM$ picture, four are upward and four are downward traveling field constituents in subdomain D_m, while in the $SHTE$ picture two upward and two downward field constituents are propagating in the same subdomain. In accordance with equations (55) and (56) $\tilde{W}^{(m)}_N$ is written as,

$$\begin{aligned} \tilde{W}^{(m;PSVTM)}_N \;=\; & \Big[\tilde{W}^{(m;-)}_{P_f}, \tilde{W}^{(m;-)}_{P_s}, \tilde{W}^{(m;-)}_{SV}, \tilde{W}^{(m;-)}_{TM}, \tilde{W}^{(m;+)}_{P_f}, \tilde{W}^{(m;+)}_{P_s}, \\ & \tilde{W}^{(m;+)}_{SV}, \tilde{W}^{(m;+)}_{TM}\Big]^T \end{aligned} \tag{70}$$

$$\tilde{W}^{(m;SHTE)}_N = \Big[\tilde{W}^{(m;-)}_{SH}, \tilde{W}^{(m;-)}_{TE}, \tilde{W}^{(m;+)}_{SH}, \tilde{W}^{(m;+)}_{TE}\Big]^T. \tag{71}$$

The imposed conditions, equations (50) and (51) on $B_J(z)$ as $|z| \to \infty$ result in,

$$\tilde{W}^{(1;-)}_r \equiv 0 \qquad \tilde{W}^{(ND;+)}_r \equiv 0 \tag{72}$$

This leaves a total of 8 $\times$ (ND-1) unknown coefficients $\tilde{W}^{(m;\pm)}_r$ (the $PSVTM$ picture) or 4 $\times$ (ND-1) unknown coefficients in the $SHTE$ picture, being just equal to the number of linear algebraic equations (60) and (61).

THE GLOBAL MATRIX METHOD

The global matrix method is used to solve simultaneously the unknown $\tilde{W}_r^{(m;\pm)}$ coefficients in all layers. The formulation was developed by Chin *et al.* (1984). The global matrix formulation has several important features: (1) multiple sources can be treated, the produced wavefields are simply superposed; (2) the up and down going wavefield coefficients are simultaneously solved for in all layers, therefore the wavefield is known to all receivers at all places in the medium for each solution pass; and (3) time stability problems do not occur because only decaying exponents are needed. In contrast, the Thomson-Haskell propagator matrix approach (Schmidt and Tango, 1986) does not have these advantageous features.

Numerical Solutions of the $PSVTM$ and $SHTE$ Problems

In the $PSVTM$ picture the eigencolumn matrix, for each subdomain m, of the system matrix $A_{I,J}^{(m;PSVTM)}$ is defined as

$$D_{J,N}^{(m;PSVTM)} = \left[\underline{\underline{d}}^{(m;-P_f,-P_s)}, \underline{\underline{d}}^{(m;-SV,-TM)}, \underline{\underline{d}}^{(m;+P_f,+P_s)}, \underline{\underline{d}}^{(m;+SV,+TM)}\right] \quad (73)$$

$$= \begin{bmatrix} M_{P,Q}^{(m,PSVTM;-)} & M_{P,Q}^{(m,PSVTM;+)} \\ N_{P,Q}^{(m,PSVTM;-)} & N_{P,Q}^{(m,PSVTM;+)} \end{bmatrix} \quad (74)$$

with $M_{P,Q}^{(m,PSVTM;\pm)}$ and $N_{P,Q}^{(m,PSVTM;\pm)}$ 4×4 matrices.

In the $SHTE$ picture the eigencolumn matrix for each subdomain m, of the system matrix $A_{I,J}^{(m;SHTE)}$ is defined as

$$D_{J,N}^{(m;SHTE)} = \left[\underline{\underline{d}}^{(m;-SH,-TE)}, \underline{\underline{d}}^{(m;+SH,+TE)}\right] = \begin{bmatrix} M_{P,Q}^{(m,SHTE;-)} & M_{P,Q}^{(m,SHTE;+)} \\ N_{P,Q}^{(m,SHTE;-)} & N_{P,Q}^{(m,SHTE;+)} \end{bmatrix} \quad (75)$$

with $M_{P,Q}^{(m,SHTE;\pm)}$ and $N_{P,Q}^{(m,SHTE;\pm)}$ 2×2 matrices.

The submatrices $\underline{\underline{d}}$ contain the eigenvectors $b_J^{(m;\pm r)}$, displacement/powerflow normalized, with $\pm r \in P_f, P_s, SV, TM$ the up and downgoing wavefield types. The propagator matrix is defined as, see equations (65) and (66),

$$\Gamma_{M,N}^{(m)} = exp[\Lambda_{M,N}^{(m)}(z_m - z_{m-1})] = \begin{bmatrix} E_{P,Q}^{(m)} & 0 \\ 0 & E_{P,Q}^{(m)-1} \end{bmatrix} \quad (76)$$

with the $E_{P,Q}^{(m)}$ matrices defined to be,

$$E_{P,Q}^{(m;PSVTM)} = diag\left(exp[-i\omega q^{(m;P_f)}\Delta z], exp[-i\omega q^{(m;P_s)}\Delta z], exp[-i\omega q^{(m;SV)}\Delta z], exp[-i\omega q^{(m;TM)}\Delta z]\right) \quad (77)$$

$$E_{P,Q}^{(m;SHTE)} = diag\left(exp[-i\omega q^{(m;SH)}\Delta z], exp[-i\omega q^{(m;TE)}\Delta z]\right). \quad (78)$$

With $q^{(m;P_f,P_s)} = \sqrt{\frac{1}{v^2_{P_f,P_s}} - p^2}$, $q^{(m;SV,SH)} = \sqrt{\frac{1}{v^2_{SV,SH}} - p^2}$, $q^{(m;TM,TE)} = \sqrt{\frac{1}{v^2_{TM,TE}} - p^2}$ the vertical slownesses for the compressional fast wave mode, the compressional slow wave mode, the vertical polarized shear wave mode, the horizontally polarized shear wave mode, the transverse magnetic EM mode, and the transverse electric EM mode. The choice of branch cuts is defined according to the computational methods used to perform the inverse Fourier and Hankel transforms:
$Im(\omega q^{(m;P_f,P_s)}) > 0$, $Im(\omega q^{(m;SV,SH)}) > 0$, $Im(\omega q^{(m;TM,TE)}) > 0$.

For $m \neq s$, see equation (60) and applying the linear transformation (69), the interface continuity condition can be written as,

$$\begin{bmatrix} M^{(m;-)}_{P,Q} & M^{(m;+)}_{P,Q} \\ N^{(m;-)}_{P,Q} & N^{(m;+)}_{P,Q} \end{bmatrix} \begin{bmatrix} E^{(m)}_{P,Q} & 0 \\ 0 & E^{(m)-1}_{P,Q} \end{bmatrix} \begin{bmatrix} \underline{p}^{(m;-)} \\ \underline{p}^{(m;+)} \end{bmatrix} - \begin{bmatrix} M^{(m+1;-)}_{P,Q} & M^{(m+1;+)}_{P,Q} \\ N^{(m+1;-)}_{P,Q} & N^{(m+1;+)}_{P,Q} \end{bmatrix} \begin{bmatrix} \underline{p}^{(m+1;-)} \\ \underline{p}^{(m+1;+)} \end{bmatrix} = \underline{0} \tag{79}$$

$$\tilde{W}^{(m;PSVTM)}_M = \begin{bmatrix} \underline{p}^{(m;PSVTM,-)} \\ \underline{p}^{(m;PSVTM,+)} \end{bmatrix}, \quad \tilde{W}^{(m;SHTE)}_M = \begin{bmatrix} \underline{p}^{(m;SHTE,-)} \\ \underline{p}^{(m;SHTE,+)} \end{bmatrix}. \tag{80}$$

Radiation Conditions

The radiation condition for halfspaces requires the conditions of no incoming waves from $|z| \to \infty$, implying $\underline{p}^{(1;-)} = 0$ and $\underline{p}^{(ND;+)} = 0$. The interface conditions at $z = z_1$ become

$$M^{(1;+)}_{P,Q} E^{(1)-1}_{P,Q} \underline{p}^{(1;+)} - M^{(2;-)}_{P,Q} \underline{p}^{(2;-)} - M^{(2;+)}_{P,Q} \underline{p}^{(2;+)} = \underline{0}$$
$$N^{(1;+)}_{P,Q} E^{(1)-1}_{P,Q} \underline{p}^{(1;+)} - N^{(2;-)}_{P,Q} \underline{p}^{(2;-)} - N^{(2;+)}_{P,Q} \underline{p}^{(2;+)} = \underline{0}.$$

At $z = z_N$ the interface conditions are,

$$M^{(ND-1;-)}_{P,Q} E^{(ND-1)}_{P,Q} \underline{p}^{(ND-1;-)} + M^{(ND-1;+)}_{P,Q} E^{(ND-1)-1}_{P,Q} \underline{p}^{(ND-1;+)} - M^{(ND;-)}_{P,Q} \underline{p}^{(ND;-)} = \underline{0}$$
$$N^{(ND-1;-)}_{P,Q} E^{(ND-1)}_{P,Q} \underline{p}^{(ND-1;-)} + N^{(ND-1;+)}_{P,Q} E^{(ND-1)-1}_{P,Q} \underline{p}^{(ND-1;+)} - N^{(ND;-)}_{P,Q} \underline{p}^{(ND;-)} = \underline{0}.$$

Free Surface Conditions

In this analysis the following matrices are used. The 3×3 matrix, $S^{(1;\mp)}_{33}$ which contains the mechanical eigenvector components that relate the mechanical wavefield amplitudes to the normal and shear bulk stresses, and to stresses in the fluid phase. The 2×3 matrix, $U^{(1;\mp)}_{23}$ which contains the mechanical eigenvector components that relate the mechanical wavefield amplitudes to the tangential magnetical and electrical wavefields. The 2×2 matrix, $V^{(1)}_{22}$ which contains the electromagnetic eigenvector components that relate the EM wavefield amplitudes to the tangential magnetical and electrical wavefields in the porous medium. The 2×1 matrix, $W^{(0;-)}_{21}$ which contains the electromagnetic eigenvector components that relate the EM wavefield amplitudes to the tangential magnetical and electrical wavefields in the upper halfspace (air). Where the superscript 1

denotes the first layer, 0 the halfspace above the free surface, and $\mp$ denotes eigenvector components relating to the down or up going wavefields.

$$S_{33}^{(1;\mp)} = \begin{bmatrix} \pm 2i\omega pq v_{p_f} G & \pm 2i\omega pq v_{p_s} G & i\omega v_{sv}\left[q^2-p^2\right] G \\ \frac{i\omega}{v_{p_f}}\left[H - 2Gp^2 v_{p_f}^2 - \frac{\left[\rho_B - \frac{H}{v_{p_f}^2}\right]}{\left[\rho_f - \frac{C}{v_{p_f}^2}\right]}\right] & \frac{i\omega}{v_{p_s}}\left[H - 2Gp^2 v_{p_s}^2 - \frac{\left[\rho_B - \frac{H}{v_{p_s}^2}\right]}{\left[\rho_f - \frac{C}{v_{p_s}^2}\right]}\right] & i\omega v_{sv}\left[q^2-p^2\right] G \\ \frac{i\omega}{v_{P_f}}\left[C - \frac{\left[\rho_B - \frac{H}{v_{p_f}^2}\right]}{\left[\rho_f - \frac{C}{v_{p_f}^2}\right]} M\right] & \frac{i\omega}{v_{P_s}}\left[C - \frac{\left[\rho_B - \frac{H}{v_{p_s}^2}\right]}{\left[\rho_f - \frac{C}{v_{p_s}^2}\right]} M\right] & 0 \end{bmatrix}$$

$$U_{23}^{(1;\mp)} = \begin{bmatrix} 0 & 0 & -\frac{i\omega LG\rho_E}{v_{sv}\rho_f}\frac{\left[\frac{1}{v_{sv}^2} - \frac{\rho_B}{G}\right]}{\left[\frac{1}{v_{sv}^2} - \epsilon\mu\right]} \\ -\frac{i\omega\rho_E Lpv_{p_f}}{\epsilon}\frac{\left[\rho_B - \frac{H}{v_{p_f}^2}\right]}{\left[\rho_f - \frac{C}{v_{p_f}^2}\right]} & -\frac{i\omega\rho_E Lpv_{p_s}}{\epsilon}\frac{\left[\rho_B - \frac{H}{v_{p_s}^2}\right]}{\left[\rho_f - \frac{C}{v_{p_s}^2}\right]} & \mp i\omega q v_{sv} LG\mu\frac{\rho_E}{\rho_f}\frac{\left[\frac{1}{v_{sv}^2} - \frac{\rho_B}{G}\right]}{\left[\frac{1}{v_{sv}^2} - \epsilon\mu\right]} \end{bmatrix}$$

$$V_{22}^{(1)} = \begin{bmatrix} -\frac{i\omega LG\rho_E}{v_{tm}\rho_f}\frac{\left[\frac{1}{v_{tm}^2} - \frac{\rho_B}{G}\right]}{\left[\frac{1}{v_{tm}^2} - \epsilon\mu\right]} & -\frac{i\omega LG\rho_E}{v_{tm}\rho_f}\frac{\left[\frac{1}{v_{tm}^2} - \frac{\rho_B}{G}\right]}{\left[\frac{1}{v_{tm}^2} - \epsilon\mu\right]} \\ -i\omega q v_{tm} LG\mu\frac{\rho_E}{\rho_f}\frac{\left[\frac{1}{v_{tm}^2} - \frac{\rho_B}{G}\right]}{\left[\frac{1}{v_{tm}^2} - \epsilon\mu\right]} & i\omega q v_{tm} LG\mu\frac{\rho_E}{\rho_f}\frac{\left[\frac{1}{v_{tm}^2} - \frac{\rho_B}{G}\right]}{\left[\frac{1}{v_{tm}^2} - \epsilon\mu\right]} \end{bmatrix}$$

$$W_{21}^{(0;-)} = \begin{bmatrix} -qv_{tm} \\ \sqrt{\frac{\epsilon}{\mu}} \end{bmatrix} \tag{81}$$

The up and downgoing mechanical wavefield amplitudes in the first layer are the fast wave amplitudes, $p_1^{(1,\pm)}$, the shear wave amplitudes, $p_2^{(1,\pm)}$, and the slow wave amplitudes, $p_3^{(1,\pm)}$, which can be related through the vanishing stress and fluid traction boundary conditions at the free surface.

$$p_{1-3}^{(1;-)} = -\left[S_{33}^{(1;-)}\right]^{-1} S_{33}^{(1;+)} p_{1-3}^{(1;+)}$$

The electromagnetic boundary conditions are the usual continuity of the magnetic, H_y, and electric, E_x, components of the electromagnetic TM mode. The radiation in the space above the free surface requires the condition of no incoming EM waves from $z \to -\infty$, implying $p_4^{(0;-)} = 0$, the TM wave downgoing amplitude is zero. The EM boundary conditions at the free surface are expressed as follows,

$$U_{23}^{(1;-)} p_{1-3}^{(1;-)} + U_{23}^{(1;+)} p_{1-3}^{(1;+)} + V_{22}^{(1)} \begin{bmatrix} p_4^{(1;-)} \\ p_4^{(1;+)} \end{bmatrix} = W_{21}^{(0;+)}. \tag{82}$$

Using equation (82), the following relation between the up and downgoing EM wave amplitudes propagating in the first layer can be obtained:

$$\begin{bmatrix} p_4^{(1;-)} \\ p_4^{(1;+)} \end{bmatrix} = \left[V_{22}^{(1)}\right]^{-1} \left(W_{21}^{(0;-)} p_4^{(0;+)} - \left[-U_{23}^{(1;-)} \left[S_{33}^{(1;-)}\right]^{-1} S_{33}^{(1;+)} p_{1-3}^{(1;+)} + U_{23}^{(1;+)} p_{1-3}^{(1;+)} \right] \right) . \quad (83)$$

Eliminating the $p_4^{(0;+)}$ amplitude , the downgoing TM amplitude in the first layer can be expressed in terms of the upgoing TM and mechanical wavefield amplitudes.

$$\begin{aligned} p_4^{(1;-)} &= \frac{1}{det(V_{22}^{(1)})} \left[\Theta \left(det(V_{22}^{(1)}) p_4^{(1;+)} + \Xi(2,1) p_1^{(1;+)} + \Xi(2,2) p_1^{(1;+)} + \Xi(2,3) p_3^{(1;+)} \right) \right. \\ &- \left. \Xi(1,1) p_1^{(1;+)} - \Xi(1,2) P_2^{(1;+)} - \Xi(1,3) p_3^{(1;+)} \right] \end{aligned} \quad (84)$$

with,

$$\Theta = \frac{V_{22}^{(1)}(2,2) W_{21}^{(0;-)}(1) - V_{22}^{(1)}(1,2) W_{21}^{(0;-)}(2)}{-V_{22}^{(1)}(2,1) W_{21}^{(0;-)}(1) + V_{22}^{(1)}(1,1) W_{21}^{(0;-)}(2)} \quad (85)$$

$$\Xi_{23} = -U_{23}^{(1;-)} \left[S_{33}^{(1;-)}\right]^{-1} S_{33}^{(1;+)} p_{1-3}^{(1;+)} + U_{23}^{(1;+)} p_{1-3}^{(1;+)} \quad (86)$$

Equations (82) and (84) relate the upgoing wave amplitudes to the downgoing wave amplitudes satisfying the free surface conditions. The downgoing wavefields reflected from the free surface are phase delayed to the next interface and included in the global boundary condition matrix. The obtained global matrix is identical in shape to the matrix obtained for a radiating upper halfspace. Inverting the global matrix yields only the upgoing wave amplitudes in the first layer. The downgoing wavefields are calculated using equations (82) and (84).

To include a source, the source jump conditions are transferred to the bottom interface of the source layer. Packing all the the interface condition equations together in a matrix, in the $PSVTM$ picture a $(ND-1)*8 \times (ND-1)*8$ dimensional and in the $SHTE$ picture a $(ND-1)*4 \times (ND-1)*4$ dimensional "global" matrix is constructed (if the medium has two radiating halfspaces). Inverting this matrix equation obtains the amplitudes for the down and up going $PSVTM$ or $SHTE$ wave amplitudes.

The system that has to be solved for is,

$$\begin{bmatrix} \underline{\underline{M}}^{(1;+)} \underline{\underline{E}}^{(1)-1} & -\underline{\underline{M}}^{(2;-)} & -\underline{\underline{M}}^{(2;+)} & & \\ \underline{\underline{N}}^{(1;+)} \underline{\underline{E}}^{(1)-1} & -\underline{\underline{N}}^{(2;-)} & -\underline{\underline{N}}^{(2;+)} & & \\ & \underline{\underline{M}}^{(s;-)} \underline{\underline{E}}^{(s)} & \underline{\underline{M}}^{(s;+)} \underline{\underline{E}}^{(s)-1} & -\underline{\underline{M}}^{(s+1;-)} & -\underline{\underline{M}}^{(s+1;+)} \\ & \underline{\underline{N}}^{(s;-)} \underline{\underline{E}}^{(s)} & \underline{\underline{N}}^{(s;+)} \underline{\underline{E}}^{(s)-1} & -\underline{\underline{N}}^{(s+1;-)} & -\underline{\underline{N}}^{(s+1;+)} \\ & & \underline{\underline{M}}^{(nd-1;-)} \underline{\underline{E}}^{(nd-1)} & \underline{\underline{M}}^{(nd-1;+)} \underline{\underline{E}}^{(nd-1)-1} & -\underline{\underline{M}}^{(nd;-)} \\ & & \underline{\underline{N}}^{(nd-1;-)} \underline{\underline{E}}^{(nd-1)} & \underline{\underline{N}}^{(nd-1;+)} \underline{\underline{E}}^{(nd-1)-1} & -\underline{\underline{N}}^{(nd;-)} \end{bmatrix} \underline{\tilde{W}} = \begin{bmatrix} \underline{0} \\ \underline{0} \\ \underline{S}^{-} \\ \underline{S}^{+} \\ \underline{0} \\ \underline{0} \end{bmatrix}$$

Chin *et al.* (1984) show that the Thomson-Haskell method (Thomson, 1950; Haskell, 1953) can be viewed as treating the coefficient matrix of the linear matrix of the linear system in a block diagonal form and applying a forward marching algorithm for its solution. This type of formulation is a shooting method for a two point boundary value problem. Gaussian elimination with partial pivoting yields stable solutions. To avoid time stability problems (exploding exponentials) the $\tilde{W}_M$ vector is multiplied with a diagonal phase matrix F_{IJ} that cancels the potentially unstable upgoing wave phase factors.

$$F_{IJ} = diag\left[E^{(1)}_{P,Q}, I_{P,Q}, E^{(2)}_{P,Q}, ..., E^{(ND)}_{P,Q}, I_{P,Q}\right] \tag{87}$$

where $I_{P,Q}$ is the identity matrix. If we define $\tilde{W}_M = F_{MN} X_N$, X_N can be shown to satisfy,

$$\begin{bmatrix} \underline{\underline{M}}^{(1;+)} & -\underline{\underline{M}}^{(2;-)} & -\underline{\underline{M}}^{(2;+)}\underline{\underline{E}}^{(2)} & & & \\ \underline{\underline{N}}^{(1;+)} & -\underline{\underline{N}}^{(2;-)} & -N^{(2;+)}_{P,Q}\underline{\underline{E}} & & & \\ & \underline{\underline{M}}^{(s;-)}\underline{\underline{E}}^{(s)} & \underline{\underline{M}}^{(s;+)} & -\underline{\underline{M}}^{(s+1;-)} & -\underline{\underline{M}}^{(s+1;+)}\underline{\underline{E}}^{(s+1)} & \\ & \underline{\underline{N}}^{(s;-)}\underline{\underline{E}}^{(s)} & \underline{\underline{N}}^{(s;+)} & -\underline{\underline{N}}^{(s+1;-)} & -\underline{\underline{N}}^{(s+1;+)}\underline{\underline{E}}^{(s+1)} & \\ & & \underline{\underline{M}}^{(nd-1;-)}\underline{\underline{E}}^{(nd-1)} & \underline{\underline{M}}^{(nd;+)} & -\underline{\underline{M}}^{(nd;-)} & \\ & & \underline{\underline{N}}^{(nd-1;-)}\underline{\underline{E}}^{(nd-1)} & \underline{\underline{N}}^{(nd-1;+)} & -\underline{\underline{N}}^{(nd;-)} & \end{bmatrix} \underline{X} = \begin{bmatrix} \underline{0} \\ \underline{0} \\ \underline{S}^{-} \\ \underline{S}^{+} \\ \underline{0} \\ \underline{0} \end{bmatrix}.$$

All terms that contained $exp[-i\omega q^{(m;P_f,P_s)}\Delta z], exp[-i\omega q^{(m;SV,SH)}\Delta z], exp[-i\omega q^{(m;TM,TE)}\Delta z]$ are eliminated. These exponentials cause numerical instability when the wavefield goes evanescent (Dunkin, 1965; Kennett, 1983; Schmidt and Tango, 1986).

POINT FORCES IN A PORO-ELASTIC STRATIFIED MEDIUM

To model a general source, the moment tensor in the poro-elastic medium needs to be determined. The following equation has to be evaluated when a cylindrical coordinate system is used,

$$\underline{h} = \underline{\underline{M}} \cdot \nabla\delta(\underline{r} - \underline{r}_s) = \begin{bmatrix} m_{rr} & m_{r\phi} & m_{rz} \\ m_{\phi r} & m_{\phi\phi} & m_{\phi z} \\ m_{zr} & m_{z\phi} & m_{zz} \end{bmatrix} \begin{bmatrix} \frac{\partial}{\partial r} \\ \frac{1}{r}\frac{\partial}{\partial\phi} \\ \frac{\partial}{\partial z} \end{bmatrix} \frac{\delta(r)}{r}\delta(\phi)\delta(z - z_s). \tag{88}$$

To simplify matters the explosion source description will be outlined. This type of source is given by,

$$\underline{h} = m\nabla\delta(\underline{r} - \underline{r}_s) = m\nabla\left[\frac{\delta(r)}{r}\delta(\phi)\delta(z - z_s)\right]. \tag{89}$$

In component form the explosion source is given by,

$$h_r = m\frac{\partial}{\partial r}\left[\frac{\delta(r)}{r}\right]\delta(\phi)\delta(z - z_s) \tag{90}$$

$$h_\phi = m\frac{\delta(r)}{r^2}\frac{\partial}{\partial\phi}\left[\delta(\phi)\right]\delta(z-z_s) \tag{91}$$

$$h_z = m\frac{\delta(r)}{r}\delta(\phi)\frac{\partial}{\partial z}\left[\delta(z-z_s)\right]. \tag{92}$$

The horizontal component of the explosion source using definition (20) reads,

$$h_V = \frac{1}{r}\left[\frac{\partial}{\partial r}(rh_r) + \frac{\partial}{\partial\phi}h_\phi\right] = m\delta(z-z_s)\nabla_1^2\left[\frac{\delta(r)\delta(\phi)}{r}\right] \tag{93}$$

The horizontal and vertical component of the explosion source after Hankel transform and mapping on a plane wave description reads,

$$\hat{h}_1 = \frac{\hat{h}_V}{i\omega p} = ikm\delta(z-z_s) \tag{94}$$

$$\hat{h}_z = m\frac{\partial}{\partial z}\delta(z-z_s). \tag{95}$$

The effect of a general point source in a stratified porous medium is accommodated by specifying a jump in the displacement stress vector B_J, across a horizontal plane containing the source (Hudson, 1969; Kennett, 1983).

To obtain this jump vector, the governing poro-elastic constitutive equations, (8) and (9), and the Fourier transformed equations of motion with an explosive point source acting on the solid frame and pore fluid in a poro-elastic medium,

$$-\omega^2\left[\rho_B\underline{u} + \rho_f\underline{w}\right] = \nabla\cdot\underline{\underline{\tau}} + m\nabla\delta(\underline{r}-\underline{r}_s) \tag{96}$$

$$-\omega^2\left[\rho_f\underline{u} + \rho_E\underline{w}\right] = -\nabla P + m\nabla\delta(\underline{r}-\underline{r}_s) \tag{97}$$

are Hankel transformed and manipulated into a set of equations that have all derivatives with respect to z on the left hand side, and a right hand side identical to the mechanical submatrix of the electroseismic system matrix (41). The first set describes the change in z of the field quantities $\left[\hat{u}_1, \hat{u}_z, \hat{w}_z, \hat{\tau}_1, \hat{\tau}_{zz}, \hat{T}_p\right]$, where the mapping given in equations (34), (35) is applied to describe the $P_f - P_s - SV$ case,

$$\frac{\partial}{\partial z}\begin{bmatrix}\hat{u}_1\\ \hat{u}_z\\ \hat{w}_z\\ \hat{\tau}_1\\ \hat{\tau}_{zz}\\ \hat{T}_p\end{bmatrix} = A_{IJ}^{(Biot;PSVTM)}\begin{bmatrix}\hat{u}_1\\ \hat{u}_z\\ \hat{w}_z\\ \hat{\tau}_1\\ \hat{\tau}_{zz}\\ \hat{T}_p\end{bmatrix} + \begin{bmatrix}0\\0\\0\\0\\m\\m\end{bmatrix}\frac{\partial}{\partial z}\delta(z-z_s) + \begin{bmatrix}0\\0\\0\\ i\omega pm\left(1-\frac{\rho_f}{\rho_E}\right)\\0\\0\end{bmatrix}\delta(z-z_s) \tag{98}$$

where $A_{IJ}^{(Biot;PSVTM)}$ is defined in equation (41). The explosion source belongs to a class of sources that are confined to a plane and arise from the transformation of some

point source leading to a dipolar contribution (Kennett, 1983). This description is given by,

$$X_I(z_s) = X_I^{(1)}\delta(z - z_s) + X_I^{(2)}\frac{\partial}{\partial z}\delta(z - z_s). \tag{99}$$

Across the source plane itself, the stress displacement vector suffers a discontinuity in the source level with a jump,

$$S_I(z_s) = \hat{\phi}(\omega)\left[B_I(z_s^+) - B_I(z_s^-)\right] = \hat{\phi}(\omega)\left[X_I^{(1)} + A_{I,J}^{(Biot;PSVTM)}(p, z_s)X_J^{(2)}\right]. \tag{100}$$

The dipolar contributions $X_I^{(1)}$ and $X_J^{(2)}$ are taken from equation (98) and $\hat{\phi}(\omega)$ is the Fourier transform of the source signature $\phi(t)$. The final jump representation of a mechanical explosive point source in a poro-elastic isotropic medium is,

$$S_I^{(P_f P_s SV)}(z_s) = \hat{\phi}(\omega)\left(\left[0, 0, 0, i\omega pm\left(1 - \frac{\rho_f}{\rho_E}\right), 0, 0\right]^T + \left[0, \frac{m}{\Delta}(M - C), \frac{m}{\Delta}\left(H - C - \frac{\Delta p^2}{\rho_E}\right), i\omega pm(\beta - \alpha), 0, 0\right]^T\right). \tag{101}$$

TRANSFORMATION BACK TO THE SPACE TIME DOMAIN

In this section, the back transformation to the space-time domain of $B_J(k, \omega, z)$, equation (69) is performed. An inverse Fourier transform is applied to go back to the time domain. An inverse Hankel transform is applied to obtain the $3D$ spatial dependence of the displacements, stresses, electric, and magnetic fields. The horizontal components of the displacements, stresses, electric, and magnetic fields require additional integration over r and ϕ to obtain, $u_r, u_\phi, \tau_{\phi z}, \tau_{rz}, H_r, H_\phi$ and E_r, E_ϕ due to the definitions of $u_V, u_H, \tau_{Vz}, \tau_{Hz}, H_V, H_H$ and E_V, E_H.

$$u_z(\omega, r, \phi, z) = \int_0^\infty kdk \sum_{n=-N}^{N}\left[J_n(kr)\hat{u}_z(\omega, k, n, z)\right]e^{in\phi}. \tag{102}$$

Identical relations exist for w_z, τ_{zz} and $T_p = -P$. The horizontal components may be recovered using the following relations:

$$u_r(\omega, r, \phi, z) = \int_0^\infty kdk \sum_{n=-N}^{N}\left[\frac{n}{kr}J_n(kr)\hat{u}_2(\omega, k, n, z) - iJ_n'(kr)\hat{u}_1(\omega, k, n, z)\right]e^{in\phi} \tag{103}$$

$$u_\phi(\omega, r, \phi, z) = \int_0^\infty kdk \sum_{n=-N}^{N}\left[\frac{n}{kr}J_n(kr)\hat{u}_1(\omega, k, n, z) + iJ_n'(kr)\hat{u}_2(\omega, k, n, z)\right]e^{in\phi}. \tag{104}$$

Identical relations exist for τ_{rz}, $\tau_{\phi z}$ in terms of $\hat{\tau}_1$ and $\hat{\tau}_2$, for E_r, E_ϕ in terms of $\hat{E}_1$ and $\hat{E}_2$ and H_r, H_ϕ in terms of $\hat{H}_1$ and $\hat{H}_2$. The above representations may be regarded as a superposition of cylindrical waves whose order dictates the nature of their

azimuthal modulation. At each frequency and angular order the radial contribution is obtained by superposing all horizontal wavenumbers k. This corresponds to including all propagating waves at the level z within the stratification, from vertically to purely horizontal traveling waves, including the evanescent waves. At any particular distance r the relative contributions of the wavenumbers are imposed by the radial phase functions $J_n(kr)$.

The integrals, (102), (103), (104) are evaluated by the discrete summation over many wavenumbers or the so-called Discrete Wavenumber Method (Bouchon and Aki, 1977).

The discretization of the radial wavenumber k in cylindrical coordinates introduces periodicity into the source distribution. The original single source problem changes after discretization into periodic concentric sources around the original source. The periodicity of these sources or the distance between two adjacent circular sources, L, is related to the discretization interval of the wavenumber, Δk, by the sampling relation,

$$L = \frac{2\pi}{\Delta k} \tag{105}$$

L and, therefore, Δk is determined by assuming a receiver located at $x_r = (r_0, z_0)$ and a source at $x_s = (0, z_s)$ on the symmetry axes of the medium configuration. Given the time window to record radiated waves from 0 to t_{max}, "pseudo" waves radiated from the periodic sources are not allowed to enter this time window. This requirement is,

$$\sqrt{(L - r_0)^2 + (z_0 - z_s)^2} > v_{fastest} t_{max} \tag{106}$$

or

$$L > r_0 + \sqrt{v_{fastest}^2 t_{max}^2 - (z_0 - z_s)^2}. \tag{107}$$

The sampling equation becomes now,

$$\Delta k < \frac{2\pi}{r_0 + \sqrt{v_{fastest}^2 t_{max}^2 - (z_0 - z_s)^2}}. \tag{108}$$

The above equation is the criterion for choosing the sample rate for the discrete wavenumber summation.

To perform the summation, the singularities of the integrands must be removed from the real k axes. This is done by adding a small imaginary part to the real frequency (analytic continuation into the complex plane), i.e. $\omega = \omega_R + i\omega_I$ with $\omega_I > 0$. If $e^{i\omega t}$ was used in the time to frequency transformation there would be a minus sign for the imaginary part of the frequency. The effect of complex frequency moves the singularities into the first and third quadrant of the complex k-plane. The use of complex frequency has the effect of smoothing the spectrum and enhancing the first motions relative to later arrivals. This effective attenuation is used to minimize the influence of the neighboring fictitious sources introduced by discrete k. The effect of the imaginary part of

the frequency can be removed from the final time domain solution by inverse complex Fourier transform with the complex frequency with the same imaginary part used in the argument of the exponential function in the Fourier transform. The magnitude of the imaginary part is usually chosen to be,

$$\omega_I = \frac{\pi}{t_{max}}. \tag{109}$$

Larger ω_I increases the attenuation for later arrivals, but also magnifies the numerical noise for late times. If ω_I is chosen too small, the attenuation may not be large enough to damp out the arrivals from the fictitious sources.

NUMERICAL ELECTROSEISMOGRAM EXAMPLES

Four different numerical models are calculated in the $PSVTM$ wavefield picture. The first example is a 100 m thick porous sand layer sandwiched in between two identical less porous halfspaces. The fluid chemistry is the same in all three layers. The source/receiver medium configuration is depicted in Figure 3. This example is meant to study electroseismic conversions as a result of a change in mechanical properties. Mechanical displacement seismograms and electroseismograms (TM mode components) are calculated and displayed in Figure 4. The converted magnetic and electric field amplitude behavior as function of antenna position are discussed for amplitudes determined at three different distances from the mechanical contrast, see Figure 5. In Figures 6 and 7, four time slice based snapshots are shown of the mechanical wavefront traversing an interface and the conversion of the mechanical wavefield into the electromagnetic TM mode components.

The second example studies the effect of a change in fluid salinity, which only affects the medium's electrical properties, on the conversion to electromagnetic waves. The source/receiver medium configuration is depicted in Figure 8. The mechanical displacement seismograms and electroseismograms (TM components) are calculated and displayed in Figure 9. The converted magnetic and electric field amplitude behavior as function of antenna position at three different distances from the electrical contrast are shown in Figure 10. The four snapshots, Figures 11 and 12 in time are calculated to trace in time the converted TM wavefield pattern generated by a mechanical wavefront traversing the electrical contrast.

The last two examples show the electroseismic effect in a Vertical Electroseismic Profiling (VESP) setting. The seismic source is located in the upper halfspace and the recording geophone/antennas are positioned vertically crossing two mechanical contrasts in the first VESP example (Figure 13) and an additional electrical contrast in the second VESP example (Figure 15).

The modeled mechanical source in all examples is a mechanical explosion source. To model true amplitudes, the diagonal elements in the seismic moment matrix, equation (88), need to be replaced by a realistic value. Using the relation $m = \frac{4\pi a^3}{3} K_G \Delta\Theta$, with a the radius of the of the nonlinear deformation zone around the source, K_G a coefficient

from the deformation equation given in equation (16), $\Delta\Theta$ the fractional change in volume and $E = \frac{4\pi a^3}{3} K_G (\Delta\Theta)^2 = \epsilon[4.7 \times 10^6 J/Kg]C$, with E the total energy, C the source weight in kilograms, and ϵ an efficiency factor expressing the fraction energy converted into sound, the following expression for m is obtained:

$$m = \sqrt{\frac{4\pi a^3}{3} K_G [4.7 \times 10^6 J/Kg] C\epsilon}. \tag{110}$$

In the numerical calculation $m = 4.4 \times 10^6 J$ is used, corresponding to $C = 1Kg$, $a = 1m$, $K_G = 10^9 Pa$ and $\epsilon = 10^{-3}$.

The Electroseismic Conversion at Mechanical Contrasts

An explosion source is positioned 100 m above the first mechanical contrast in the upper halfspace. Fifteen receivers are positioned symmetrically in a straight horizontal line at both sides of the source 95 m above the interface. The receiver spacing is 10 m. The medium parameters of the two halfspaces and the 100 m thick sand layer are given in Table I. Based on these medium properties the mechanical fast wave, slow wave, shear wave, and electromagnetic TM wave velocities are calculated. The complex velocities and calculated bulk conductivities are given in Table II. A slow wave and TM wave velocity range is given since these two wave phenomena are diffusive.

When an explosion source is set off, only P waves are generated in an isotropic poroelastic medium. Numerically the 8×1 displacement-stress-EM wavefield component vector is calculated at each geophone/antenna position. In Figure 4 only the mechanical displacement seismograms (u_z and u_x components) and the electroseismograms (TM mode components) are shown. All plots are seismogram scaled. The amplitudes of the first 40 $msec$ in the E_x and H_y electroseismograms are multiplied by a factor 50 to enhance the electroseismic converted field generated at the first interface.

At the mechanical contrast, the P wave reflects as a P wave, a converted SV wave, and a converted TM wave. The direct wave is omitted in all seismograms. The mechanical seismograms show the PP reflection and PSV conversion generated at the top and bottom of the thick sand layer. The converted TM wavefield components show up at all antennas at approximately half the two way P wave traveltime for normal incidence reflection. Since the TM wavefield velocity is at least two orders of magnitude faster than the P wavefield (Table II), the traveltime spent by the TM waves in traveling upward to the antennas is negligable and the total two way traveltime appears to coincide with the one way traveltime of the incoming P wave at normal incidence reflection. The hyperbolas arriving at a later time in the E_x and H_y electroseismograms have the same traveltime as the PP reflection (compare the mechanical seismogram with the E_x electroseismogram in Figure 4 and the same traveltime as the PSV conversion (compare mechanical seismogram with the H_y electroseismogram), respectively.

In the first case, the compressional waves traveling through a homogeneous porous medium cause pressure gradients which cause the charge to separate. This induces

within the seismic pulse a system of electric fields that travel with the compressional wave speed. As explained before, the seismic pulse doesn't radiate electromagnetic fields away from the pulse. Therefore, when the reflected P wave pulse passes the antennas, an electric field is registered inside the P wave pulse. In the second case the vertical polarized rotational mechanical waves traveling through a homogeneous porous medium cause grain accelerations, setting up current sheets. This induces within the seismic pulse magnetic fields that travel with rotational mechanical wave speed. Therefore, when the converted SV wave pulse passes the antennas, a magnetic field is recorded inside the SV wave pulse. The electric and magnetic field strengths in the seismic pulse are in this case larger than the converted TM wavefield components strengths. The E_x hyperbolas arriving after the electroseismic conversion are associated with the electric fields inside the P wave pulse traveling with fast wave velocity. While the H_y hyperbolas arriving after the electroseismic conversion are associated with the magnetic fields inside the SV wave pulse traveling with S wavespeed velocity. The TM conversions from the bottom mechanical contrast have amplitudes which are too small to be identified in the electroseismogram with the scaling used.

In Figure 5, the converted electric and magnetic absolute field amplitudes versus antenna offsets are shown at 20, 50 and 95 m from the interface. The field amplitude at each antenna position is determined by calculating a root mean square amplitude inside an estimated pulse window in the time domain. The converted TM wavefield, driven by the seismic pulse frequency, is diffusive, the real and imaginary parts of the TM velocity are almost equal, and therefore the largest signals are measured by antennas closest to the interface. The frequency content of the electromagnetic field is the same as the frequency content of the incident seismic wave. Since we are in the, $\frac{\sigma}{\omega\epsilon} >> 1$, conducting medium regime, we can find a skindepth $\delta = \sqrt{\frac{2}{\omega\mu_0\sigma}}$, with $\mu_0 = 4\pi \times 10^{-7}$ (Kong, 1990, p. 60), the permeability of the medium. If the propagation distance is much less than the skindepth, the near field of the radiating interface, then the frequency content in the mechanical and electromagnetic field are the same. The increase in amplitude with increasing source-antenna offset and a later decay in amplitude with offset show similarities with amplitudes that would be recorded if the interface was replaced by a seismically induced electric dipole right under the source.

To investigate the TM wavefield conversions in more detail, snapshots in time are calculated around the first mechanical contrast. In Figures 6 and 7, four successive time snapshots are displayed, showing the mechanical u_z wavefield component, the top figure, the electromagnetic H_y component, the middle figure, and the electromagnetic E_x component, bottom figure at 26.6 $msec$, 28.9 $msec$, 30.5 $msec$ and 32.0 $msec$ after the shot, respectively. The wavefields are determined at 120 by 60 receiver/antenna positions. The receiver/antenna spacings are 1 m in the horizontal direction and 3 m in the vertical direction. At $t = 26.6$ $msec$, the Ricker wavelet (Hosken, 1988) front has reached the interface at -90 m (Figure 6, left column). The $t = 26.6$ $msec$ snapshot displaying the magnetic field component of the TM mode shows, with a position centered under the seismic source at distance 60 m, an amplitude radiation pattern of an

equivalent magnetic current loop with field lines pointing at one side into the paper and at the other side out of the paper. The magnetic field diffuses with large velocity away from the interface. The $t = 26.6$ $msec$ snapshot displaying the electric field component of the TM mode shows an amplitude radiation pattern of an electric dipole, positioned right under the seismic source at a distance 60 m. The largest electric fields are associated with the field inside the P wave pulse. At later times, when a larger part of the seismic pulse has traversed the interface, the magnetic current loop diameter increases and the TM wavespeed differences above and below the interface becomes visible. The current system imbalances across the interface change in direction in accordance with the pulse polarity, the magnetic and electric field polarities flip accordingly. The last two snapshots show complex patterns of mechanical field convergences into electromagnetic fields. More than one magnetic current loops appear with alternating field line directions and the inner loop diameter increases. Also more electric dipoles with opposite "dipole type moments" appear there where the wavefront passes. The combined E_x and H_y amplitude pattern away from the interface has a predominant effective electrical dipole character, or its dual, an effective magnetic current loop character away from the interface. In both cases the amplitudes decay fast with traveled distance.

The Electroseismic Conversion at Electrical Contrasts

The explosion source is again positioned 100 m above an electrical contrast in the upper halfspace. Fifteen receivers are positioned symmetrically in a straight horizontal line at both sides of the source 95 m above the interface to record the reflection from the contrast and 95 m below the interface to record the transmissions through the contrast. The receiver spacing is 10 m. The medium input parameters describing the two halfspaces are given in Table I. The calculated medium velocities and bulk conductivities based on the medium parameters listed in Table I are shown in Table III.

In Figure 9, the mechanical displacement seismograms (u_z and u_x components) and the electroseismograms (TM mode components) are shown. All four plots are seismogram scaled. At the electrical contrast the P wave reflects only as converted TM waves. Since there is no mechanical contrast, the P wave does not reflect or convert into shear waves. The mechanical u_x and u_z seismograms show the transmitted wavefields through the electrical contrast at the geophones 95 m below the interface which are essentially the direct P wavefield from the explosion source in the upper halfspace. The TM wavefield components are recorded at antennas at approximately the one way P wave traveltime from source to interface. Since the direct wave in the upper halfspace is omitted, the E_x wavefield seismogram does not show induced electric fields within the seismic pulse that travel with the compressional wave speed.

In Figure 10, the converted electric and magnetic absolute field amplitudes versus antenna offsets are shown at 20, 50 and 95 m from the interface. An increase in amplitude with increasing source-antenna offset up to a global maximum is observed. When the source-antenna offset is further increased, the amplitudes decrease monotonically. The amplitude pattern shows similarities with amplitudes that would be recorded if the

interface had been replaced by a seismically induced electric dipole or magnetic loop centered right under the seismic source. If Figures 5 and 10 are compared, the field amplitude curves have similar shape. The amplitudes, however, are a factor 10 bigger for the converted TM mode generated at the electrical contrast when compared to the converted TM mode amplitudes converted at the electrical contrast.

In Figures 11 and 12, four successive snapshots in time are displayed, showing the mechanical u_z wavefield component, top figure, the electromagnetic H_y component, middle figure, and the electromagnetic E_x component, bottom figure at 26.6 $msec$, 28.9 $msec$, 30.5 $msec$ and 32.0 $msec$ after the shot, respectively. The number of geophones/receivers and their spacings in horizontal and vertical directions are identical to the mechanical contrast case. The top halfspace has a salinity of 1.0 mol/l and the lower halfspace has a salinity of 0.001 mol/l. This results in a larger conductivity and lower electromagnetic wavefield velocity in the upper halfspace than in the lower halfspace (Table III). Therefore, the electric fields within the incoming seismic P wave pulse are small in amplitude when compared to the electric fields within the mechanical P wave in the lower halfspace. This amplitude behavior can be clearly observed in the electromagnetic E_x component snapshots. Tracing the transient TM component wavefield pattern fronts in Figures 11 and 12, the TM wavefield velocity difference in both halfspaces is evident. The complex convergence patterns from mechanical wavefield into electromagnetic TM fields are similar to the patterns observed around the mechanical contrasts (compare Figures 6 and 7 with 11 and 12). The resultant E_x and H_y amplitude pattern away from the interface has again a predominant effective electrical dipole character or its dual an effective magnetic current loop character which are centered under the source at the contrast's depth. The amplitudes of the TM mode transients decay rapidly with traveled distance.

Vertical Electroseismic Profiling (VESP)

The converted TM mode amplitude behavior with distance, discussed when the surface electroseismic calculations were discussed, suggests that the VESP geometry setting can be an important one. Since with this technique the antennas are positioned close to the target of interest, larger converted electromagnetic signals can be recorded before they become too attenuated with distance. With the VESP technique the electroseismic method can be applied to targets, electrical and/or mechanical contrasts, at greater depths.

The first VESP example is a three layer model with the first interface at 300 m depth and the second interface at 400 m depth. The first receiver/antenna is positioned at a horizontal offset of 50 m and a depth of 155 m. The receiver/antenna depth spacing is 10 m. The medium description with its most important electroseismic medium parameters is shown in Figure 13. In Figure 14, the numerically calculated VESP's are shown. The top plot is the mechanical displacement response, and the middle and bottom plots show the E_x and H_y TM mode components, respectively. The top VESP in Figure 14 shows the P wave reflections and converted SV wave reflection at the top and bottom

interface of the "sand reservoir." The direct P wave in the top halfspace is omitted. The other two vertical electroseismic profiles show the converted TM mode components at the two contrasts. The converted TM wavefield components show up at all antennas at virtually the same time. The high electrical conductivity in the middle layer attenuates the electric field amplitudes completely. The later arrivals in the E_x VESP are electric fields within the seismic pulse that travel with the compressional wave speed. The H_y component VESP shows the fast decay of the converted electroseismic fields with distance. The converted H_y component of the TM mode is much larger in amplitude than the induced magnetic fields inside the SV wave pulse. The main reason is the close antenna position to the target of interest.

The last numerical example has a new electrical contrast added to the previous model, see Figure 15. The 100 m thick "reservoir sand" is now divided into two sands with identical mechanical properties saturated with two fluids of different salinity. In Figure 16, the calculated VESP's are shown. The mechanical displacement response is identical to the previous calculation without the electrical contrast. But the TM mode component VESP's are modified with an extra electroseismic conversion at the electrical contrast.

CONCLUSIONS

A global matrix method is described which solves the macroscopic governing equations controlling the coupled electromagnetics and acoustics of porous media numerically in layered poro-elastic media driven by arbitrary seismic point sources. The coupled equations decouple into a $PSVTM$ and a $SHTE$ picture. The induced current motion plane determines to which electromagnetic mode the mechanical waves are coupled. Seismic motion which generates relative flow, induces a "streaming" electrical current due to cation motion. The driving force for the relative flow is a combination of pressure gradients set up by the peaks and throughs of a compressional wave and by grain accelerations. The relative flow and therefore current can be both due to compressional and shear waves.

Compressional waves traveling through homogeneous porous medium cause pressure gradients which cause the charge to separate. This induces within the seismic pulse a system of electric fields that travel with the compressional wavespeed. Rotational waves traveling through a homogeneous porous medium cause grain accelerations and set up current sheets. This induces within the seismic pulse magnetic fields that travel with the rotational wavespeed. Therefore, when the seismic pulse passes an antenna, an electric field is recorded inside the P wave pulse and a magnetic field is recorded inside the S wave pulse. The seismic pulse doesn't radiate electromagnetic waves away from the pulse.

Radiating electromagnetic wavefields are converted from seismic waves, however, when contrasts in mechanical and/or electrical properties are traversed. The principal features of the converted electromagnetic signals are: (1) contacts all antennas at ap-

proximately the same time; (2) arrives at the antennas at half of the seismic traveltime at normal incidence reflected P waves; and (3) changes sign on opposite sides of the shot. The frequency content of the converted electromagnetic field has the same frequency content of the driving incident seismic pulse, as long as the propagation distances are much less than the electromagnetic skin depth.

Root mean square converted electromagnetic amplitudes versus seismic point source-antenna offset are calculated for a mechanical porosity contrast and an electrical, salinity contrast at different depths. The amplitude curves are similar in shape, first a strong increase in amplitude to a global maximum is observed with increasing antenna offset and next a monotonic decrease in amplitude with increasing antenna offset. The amplitudes decrease rapidly with traveled distance.

Four snapshots in time show the wavefield there where the seismic wavefront passes the interface creating current imbalances across the interface. Equivalent sources can be identified with the conversion to electromagnetic waves. A magnetic current loop can be identified with the H_y component snapshots and electric current dipoles can be identified with the E_x snapshots. The total conversion to electromagnetic waves can be either represented by an effective current dipole or an effective magnetic loop since they are each others dual. The TM component amplitude radiation patterns recorded at some distance from the interface show similarities with the wavefield that would be obtained if the interface was replaced by an equivalent electric dipole or magnetic current loop positioned right beneath the seismic source at the contrast's depth. The amplitude versus offset results and the electroseismograms confirm such an effective conversion right beneath the source. The VESP modeling shows the rapid decay of the converted electroseismic signals with distance. The antennas close to the target of interest show larger amplitudes in the converted signal than electromagnetic signals inside the seismic pulse. With increasing distance to the antenna, the electromagnetic signal inside the seismic pulse totally dominates the converted fields in the electroseismograms.

ACKNOWLEDGMENTS

This research is supported by the Department of Energy, Office of Energy Research, grant number DE-FG02 -93ER14322. We would like to thank Dr. Chengbin Peng for his helpful discussions regarding the Global Matrix method. The first author was sponsored by an OYO fellowship.

REFERENCES

Biot, M. A., Mechanics of deformation and acoustic propagation in porous media, *J. Applied Physics, 33,* 1482–1498, 1962.

Bockris, J. O. and A. K. N. Reddy, *Modern Electrochemistry,* vol. 2, Plenum Press, 1970.

Bouchon, M. and K. Aki, Discrete-wavenumber representation of seismic source wavefields, *Bull. Seis. Soc. Am., 67,* 259–277, 1977.

Chin, R. C. Y. , G. W. Hedstrom, and L. Thigpen, Matrix methods in synthetic seismograms, *Geophys. J. Roy. astr. Soc., 77,* 483–502, 1984.

Dunkin, J. W. , Computation of modal solutions in layered, elastic media at high frequencies, *Bull. Seis. Soc. Am., 55,* 335–358, 1965.

Gaudin, A. and D. Fuerstenau, Quartz flotation with anionic collectors, *Trans AIME,* 66–72, 1955.

Haartsen, M., Coupled electromagnetic and acoustic wavefield modelling in poro-elastic media and its applications in geophysical exploration, Ph.D. thesis, Massachusetts Institute of Technology, Cambridge, MA, 1995.

Hosken, J., Ricker wavelets in their various guises, *First Break, 6,* 25–33, 1988.

Hudson, J. A., A quantitative evaluation of seismic signals at teleseismic distances i-radiation from a point source, *Geophys. J. Roy. astr. Soc., 18,* 133–249, 1969.

Johnson, D. L., J. Koplik, and R. Dashen, Theory of dynamic permeability and tortuosity in fluid-saturated porous media, *J. Fluid Mechanics,* 379–402, 1987.

Kennett, B. L. N., *Seismic Wave Propagation in Stratified Media,* Cambridge University Press, 1983.

Kong, J., *Electromagnetic wave theory,* Wiley and Sons, Inc., 1990.

Mal, A., Guided waves in layered solids with interface zones, *Int. J. Eng. Sci., 26,* 873–881, 1988.

Mal, A., Wave propagation in layered composite laminates under periodic surface loads, *Wave Motion, 10,* 257–266, 1988.

M.P. Sidorova, M. F., and D. Fridrikhsberg, *Electrokinetic studies of some model systems: quartz-electrolyte solutions in Wolfram,* Proc. Inter. Conf. Colloid Surf. Sci., Elsevier Science Publ. Co., 1975.

Pride, R. S., A. F. Gangi, and F. D. Morgan, Deriving the equations of motion for porous isotropic media, *J. Acoust. Soc. Am., 92,* 1992.

Pride, S., Governing equations for the coupled electromagnetics and acoustics of porous media (submitted), *Phys. Rev. B,* 1994.

Hidalgo-Alvarez, R. and G. Pardo, Comparative sedimentation and streaming potential studies for ζ potential determination, *J. Colloid and Interface Sci., 107,* 295–300, 1985.

Schmidt, H. and G. Tango, Efficient global matrix approach to the computation of synthetic seismograms, *Geophys. J. Roy. Astron. Soc., 84,* 331–359, 1986.

Watson, G. N., *A Treatise on the Theory of Bessel Functions*, (2nd edition), Cambridge University Press, 1966.

TABLE I. The mechanical contrast and the electrical contrast medium properties.

Property	Top and bottom halfspaces	Sand layer	Fresh water halfspace	Brine halfspace
porosities ($\phi[\%]$)	15	30	15	15
dc permeability ($k[m^2]$)	10^{-12}	10^{-12}	10^{-12}	10^{-12}
bulk modulus solid ($k_s[Pa]$)	3.6×10^{10}	3.6×10^{10}	3.6×10^{10}	3.6×10^{10}
bulk modulus fluid ($k_f[Pa]$)	2.2×10^{9}	2.2×10^{9}	2.2×10^{9}	2.2×10^{9}
frame bulk modulus ($k_{fr}[Pa]$)	9.9×10^{9}	9.9×10^{9}	9.9×10^{9}	9.9×10^{9}
frame shear modulus ($g_{fr}[Pa]$)	9.0×10^{9}	9.0×10^{9}	9.0×10^{9}	9.0×10^{9}
fluid viscosity ($\eta[Pas]$)	1.0×10^{-3}	1.0×10^{-3}	1.0×10^{-3}	1.0×10^{-3}
density solid ($\rho_s[Kg/m^3]$)	2.7×10^{3}	2.7×10^{3}	2.7×10^{3}	2.7×10^{3}
density fluid ($\rho_f[Kg/m^3]$)	1.0×10^{3}	1.0×10^{3}	1.0×10^{3}	1.0×10^{3}
salinity ($C[mol/l]$)	1.0×10^{-3}	1.0	1.0×10^{-3}	1.0
temperature ($T[K]$)	298	298	298	298
permittivity (κ_f)	80	80	80	80
permittivity (κ_s)	4	4	4	4
tortuosity (α_∞)	3	3	3	3

TABLE II. Calculated wavefield velocities and bulk conductivities used in the mechanical contrast model.

Properties	Upper and lower halfspace	Sand reservoir layer
fast wave velocity$[m/s]$	(3282.62, -0.1037)	(3158.56, -0.7419)
slow wave velocity$[m/s]$	(21.2/146.2, -13.3/-119.1)	(16.7/111.6, -10.5/-100.3)
shear wave$[m/s]$	(1769.14, -1.39)	(1669.25, -1.53)
TM wave velocity$[m/s]$	(318890/2.04 10^6, -201223/-2.02 10^6)	(7159/45665, -4517/ -45326)
conductivity ($\sigma[S/m]$)	0.000388	0.77

TABLE III. Calculated wavefield velocities and bulk conductivities used in the electrical contrast model.

Properties	Top fresh water saturated halfspace	Bottom brine saturated halfspace
fast wave velocity$[m/s]$	(3282.62, -0.1037)	(3282.62, -0.1037)
slow wave velocity$[m/s]$	(21.2/146.2, -13.3/-119.1)	(21.2/146.1, -13.3/-119.1)
shear wave$[m/s]$	(1769.14, -1.39)	(10124.4, -6388.66) - (64579.9, -64100.4)
TM wave velocity$[m/s]$	(318890/2.04 10^6, -201223/-2.02 10^6)	(10124/64580, -6389/-64100)
conductivity ($\sigma[S/m]$)	0.000388	0.385

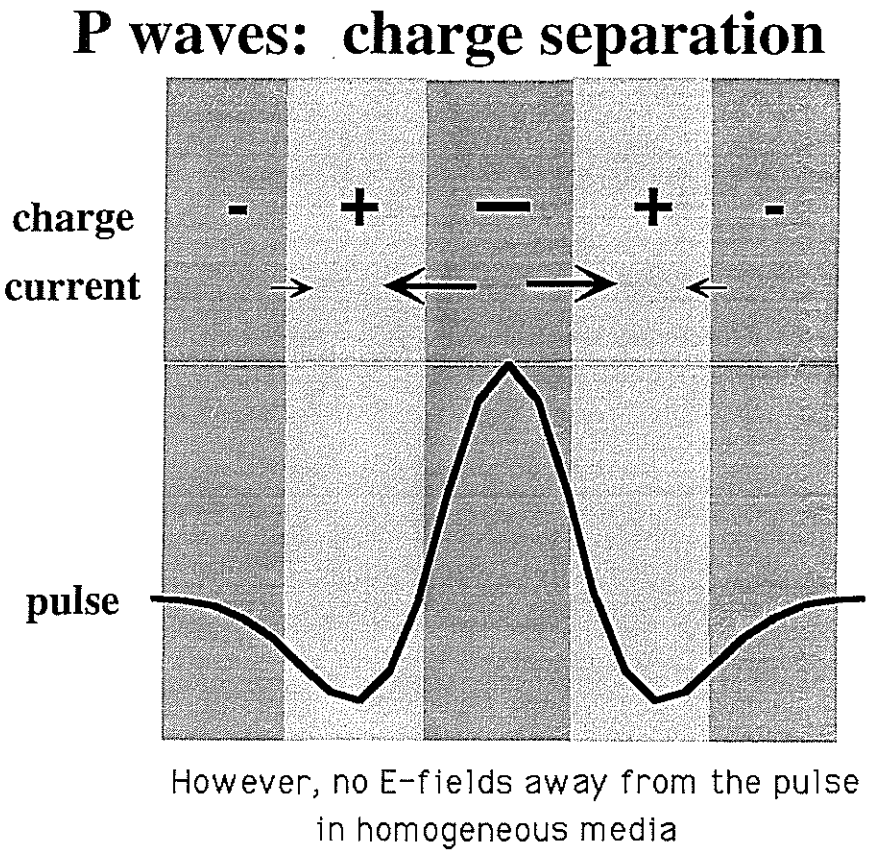

Figure 1: Electric fields due to charge separation within a P wave seismic pulse.

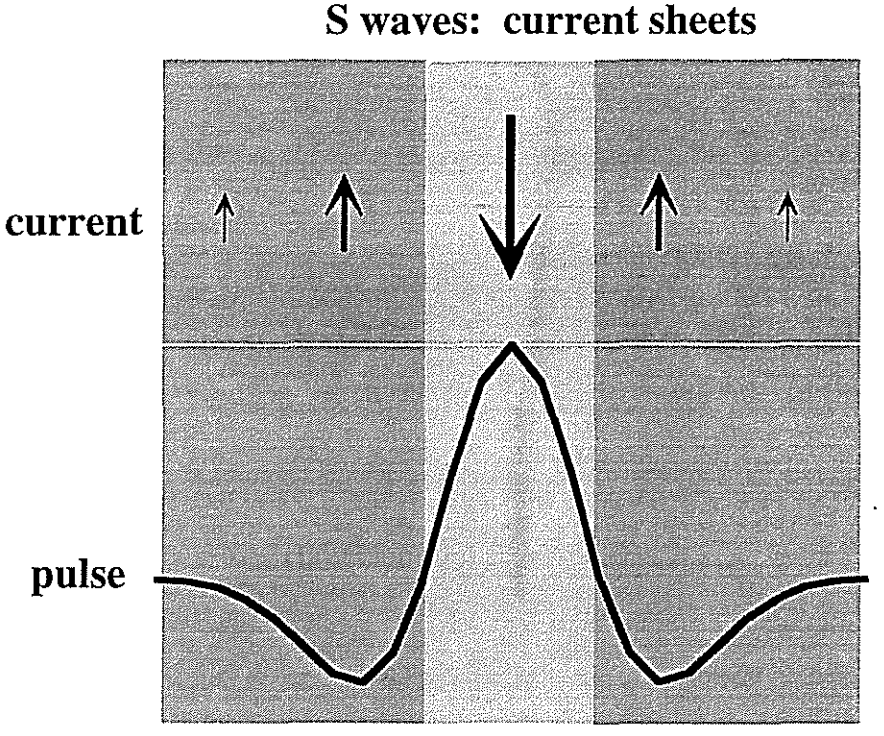

Figure 2: Magnetic fields due to current sheets within a SV wave seismic pulse.

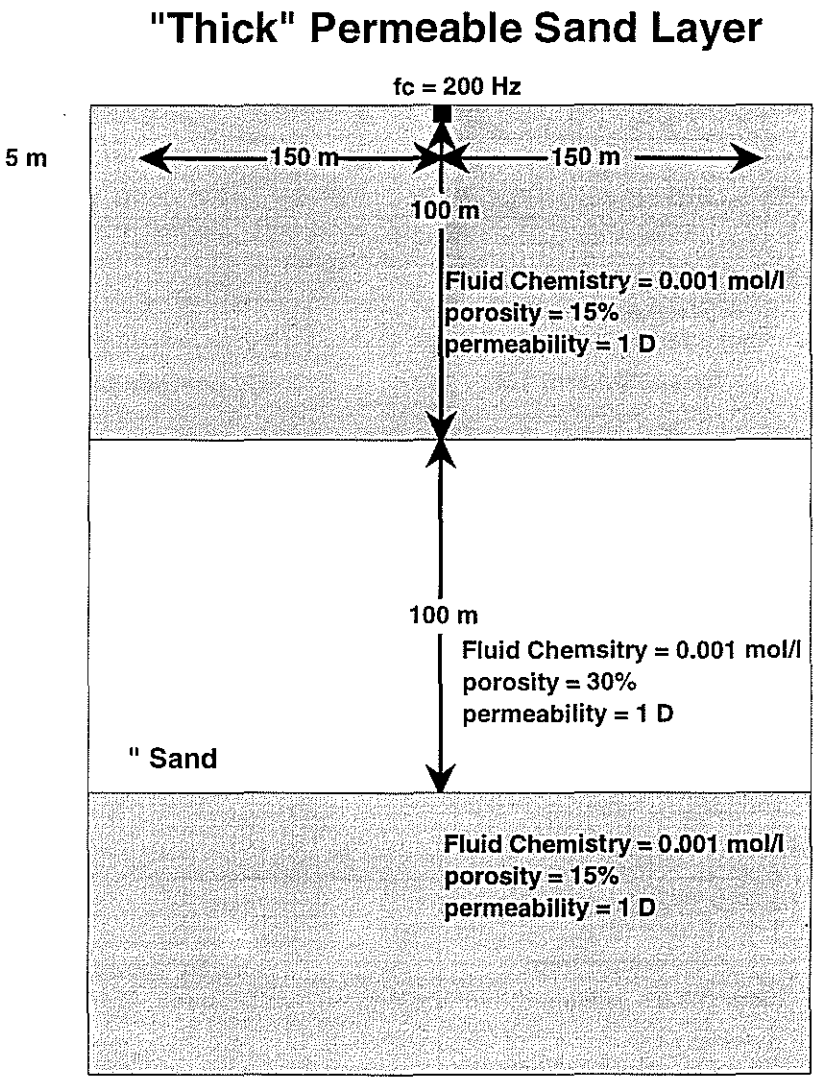

Figure 3: The thick permeable sand medium configuration.

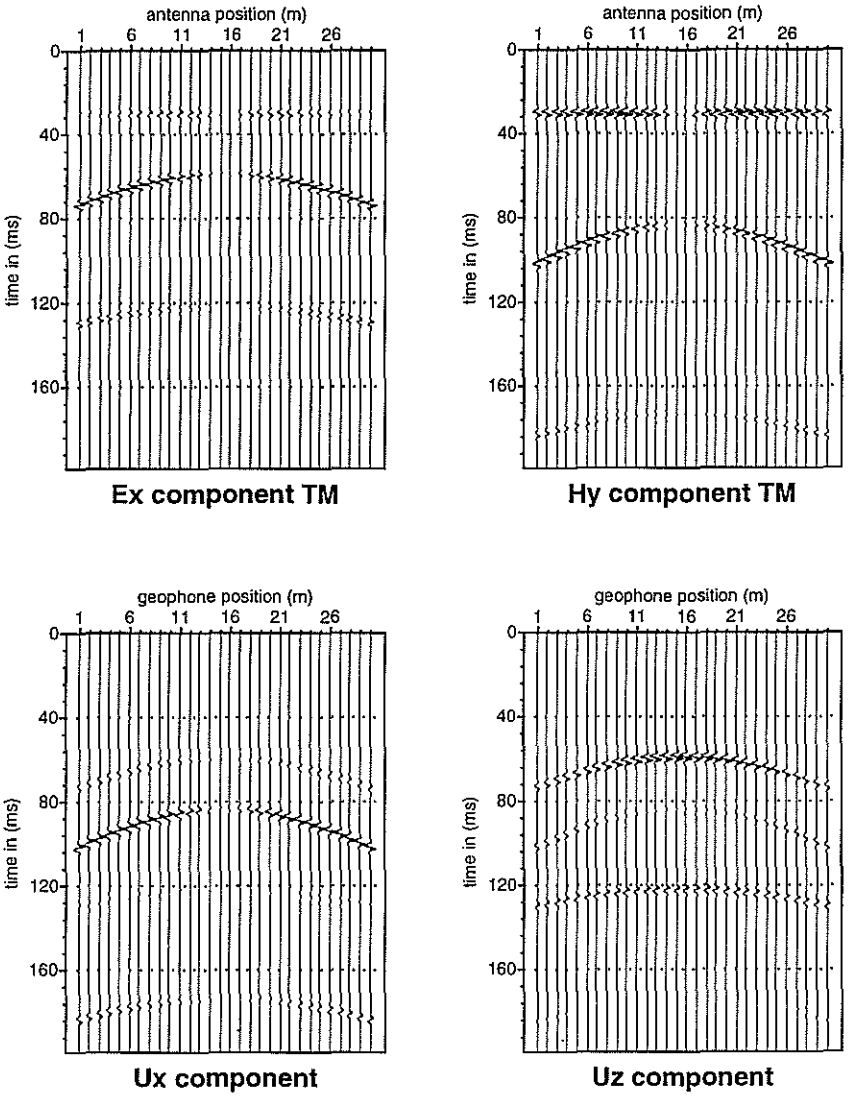

Figure 4: The mechanical displacement component seismograms and the TM mode component electroseismograms calculated for the thick permeable sand medium configuration.

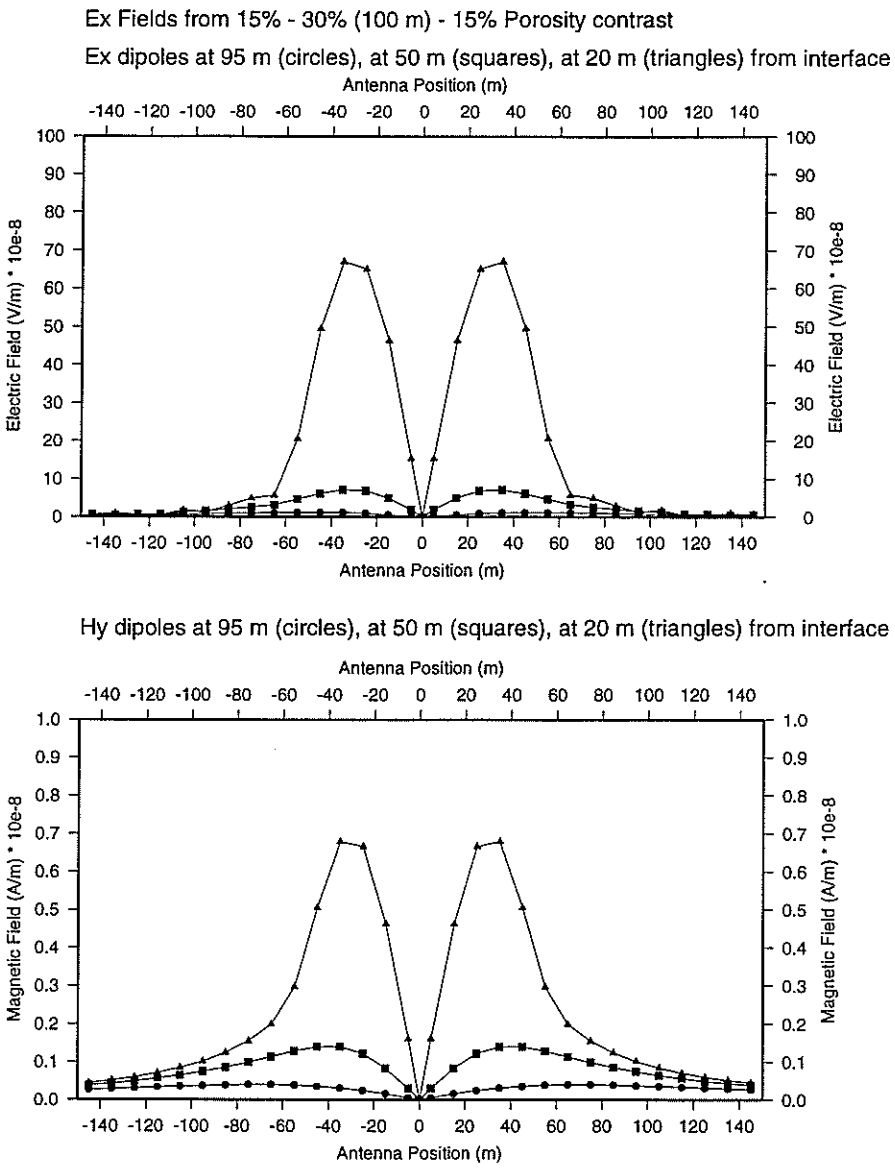

Figure 5: Converted electric and magnetic root mean square wavefield amplitudes versus antenna offsets calculated at 20, 50 and 95 m from a mechanical contrast generated by an explosive point source.

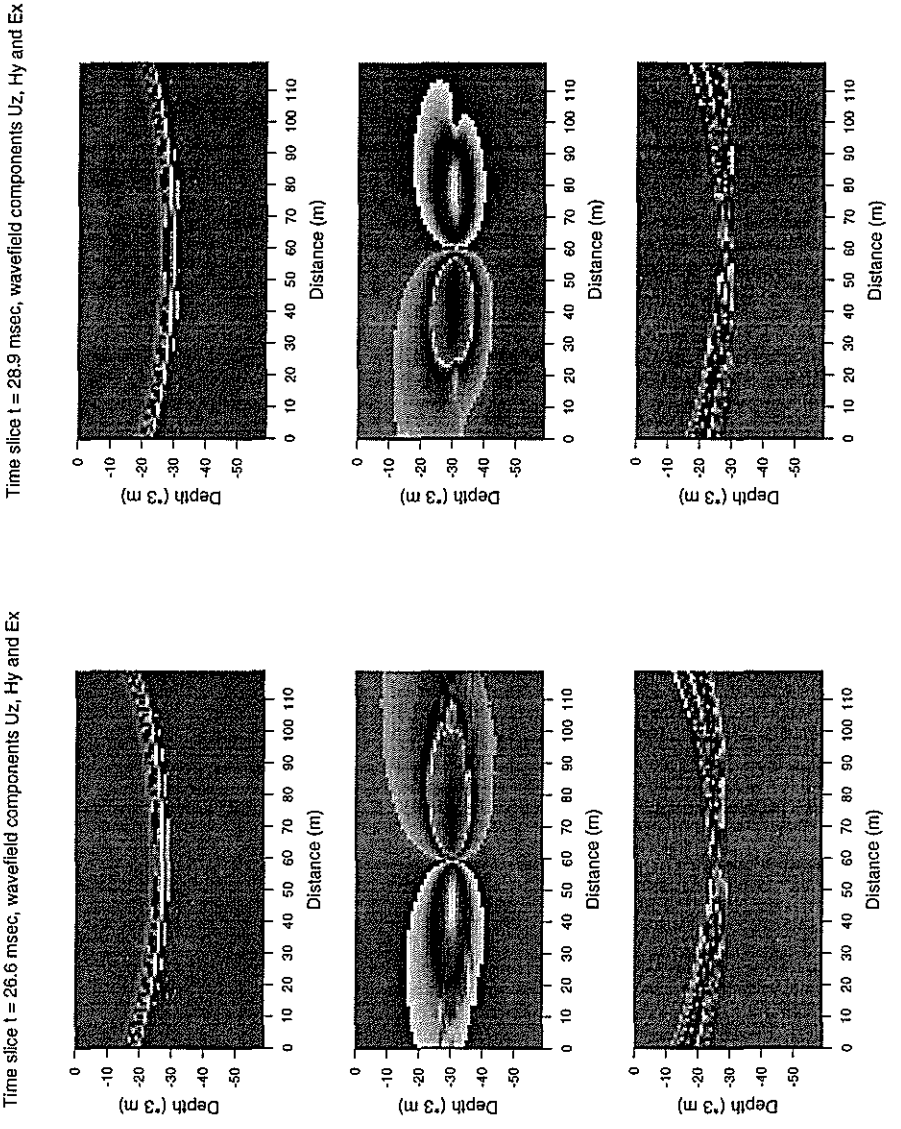

Figure 6: Time slice snapshots calculated at 120 by 60 geophone/receiver positions around a mechanical contrast at $t = 26.6$ *msec* and $t = 28.9$ *msec* after explosion. Top snapshot is u_z component of mechanical displacement wavefield, middle snapshot is H_y component of electromagnetic TM mode, bottom snapshot is E_x component of electromagnetic TM mode.

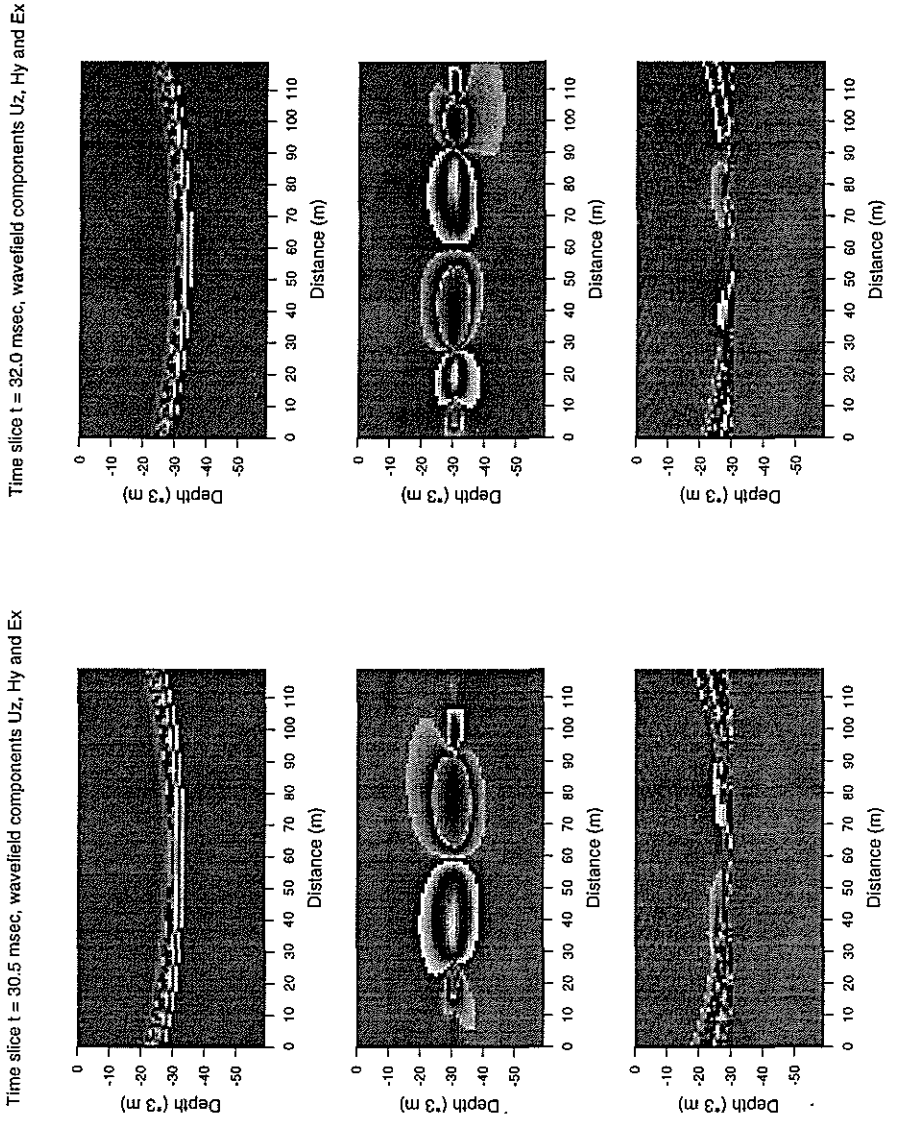

Figure 7: Time slice snapshots calculated at 120 by 60 geophone/receiver positions around a mechanical contrast at $t = 30.5$ $msec$ and $t = 32.0$ $msec$ after explosion. Top snapshot is u_z component of mechanical displacement wavefield, middle snapshot is H_y component of electromagnetic TM mode, bottom snapshot is E_x component of electromagnetic TM mode.

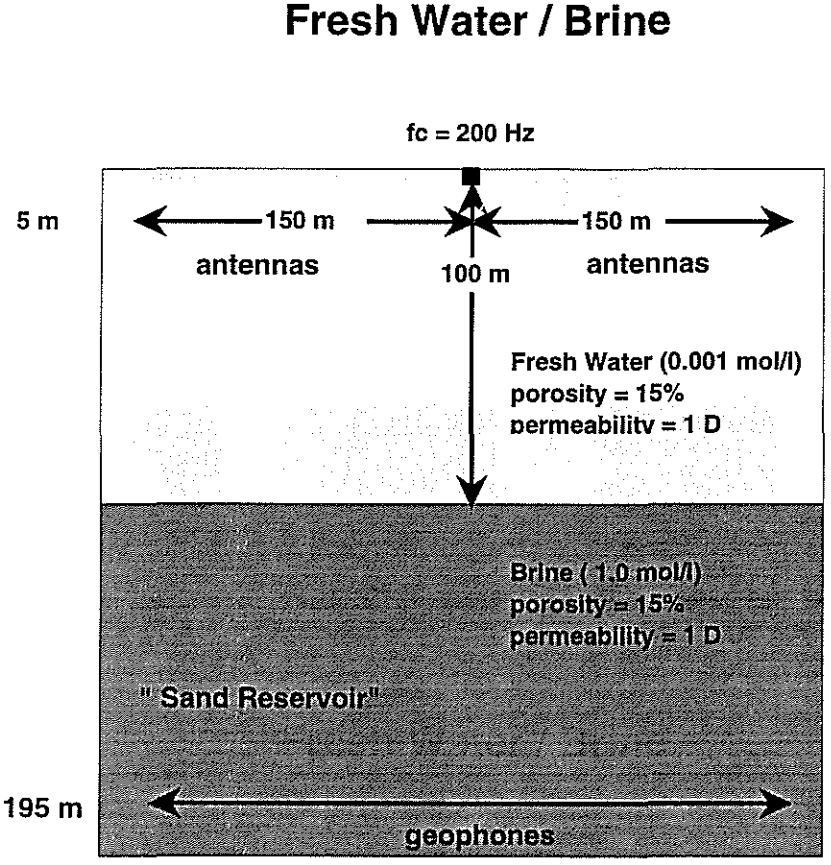

Figure 8: The fresh water-brine medium configuration.

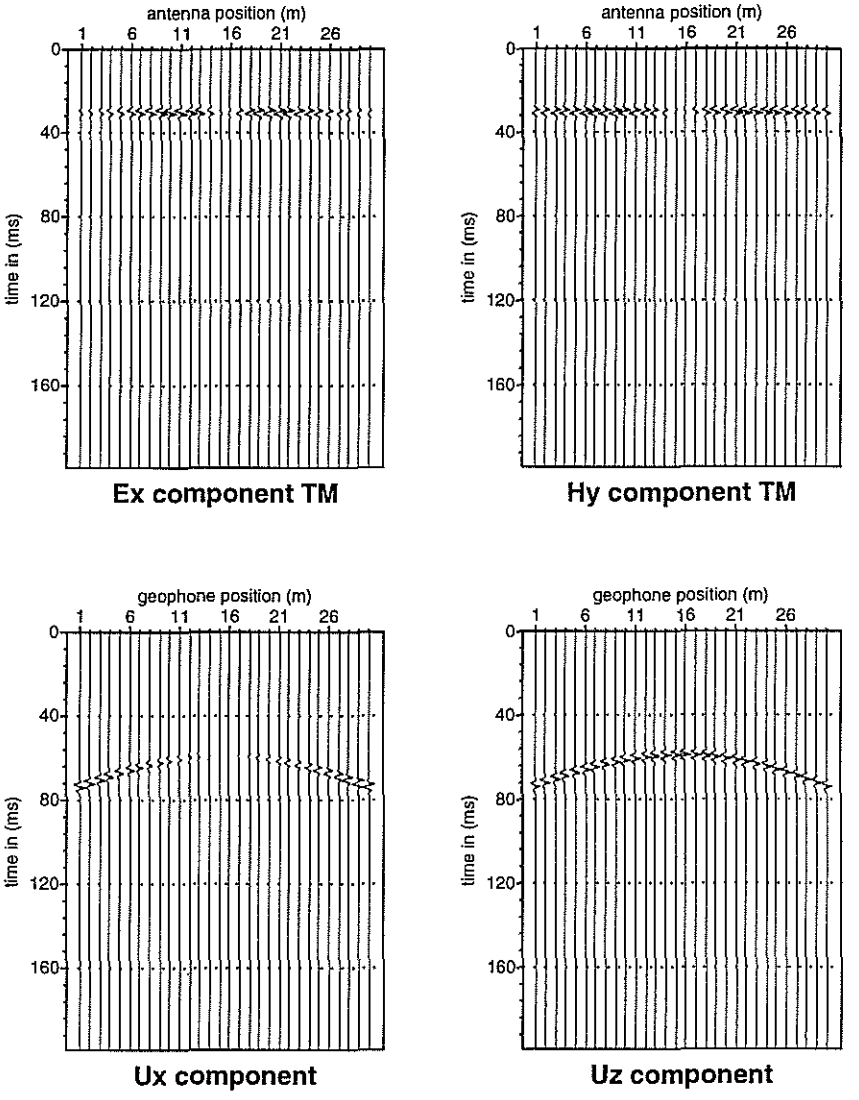

Figure 9: The mechanical displacement component seismograms and the TM mode component electroseismograms calculated for the fresh water-brine medium configuration.

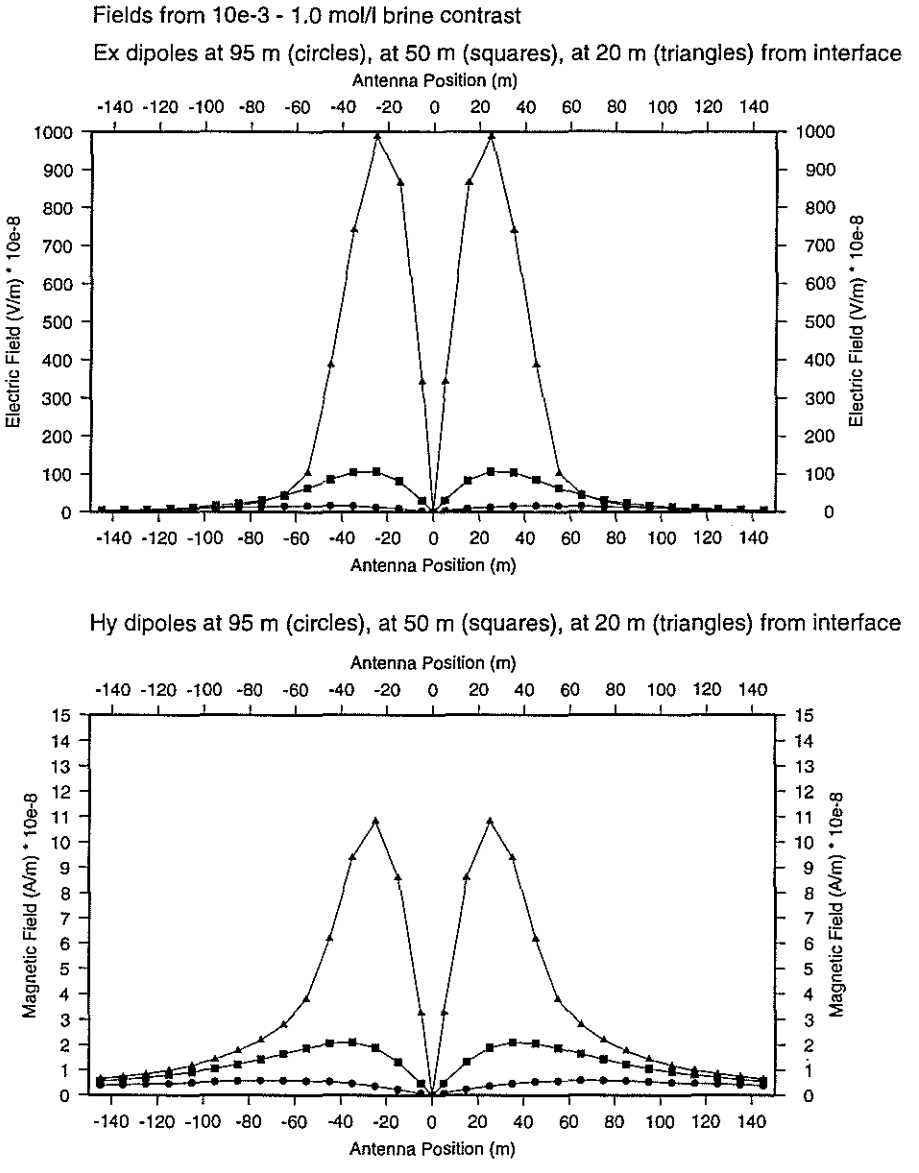

Figure 10: Converted electric and magnetic root mean square wavefield amplitudes versus antenna offsets calculated at 20, 50 and 95 m from an electrical contrast generated by an explosive point source.

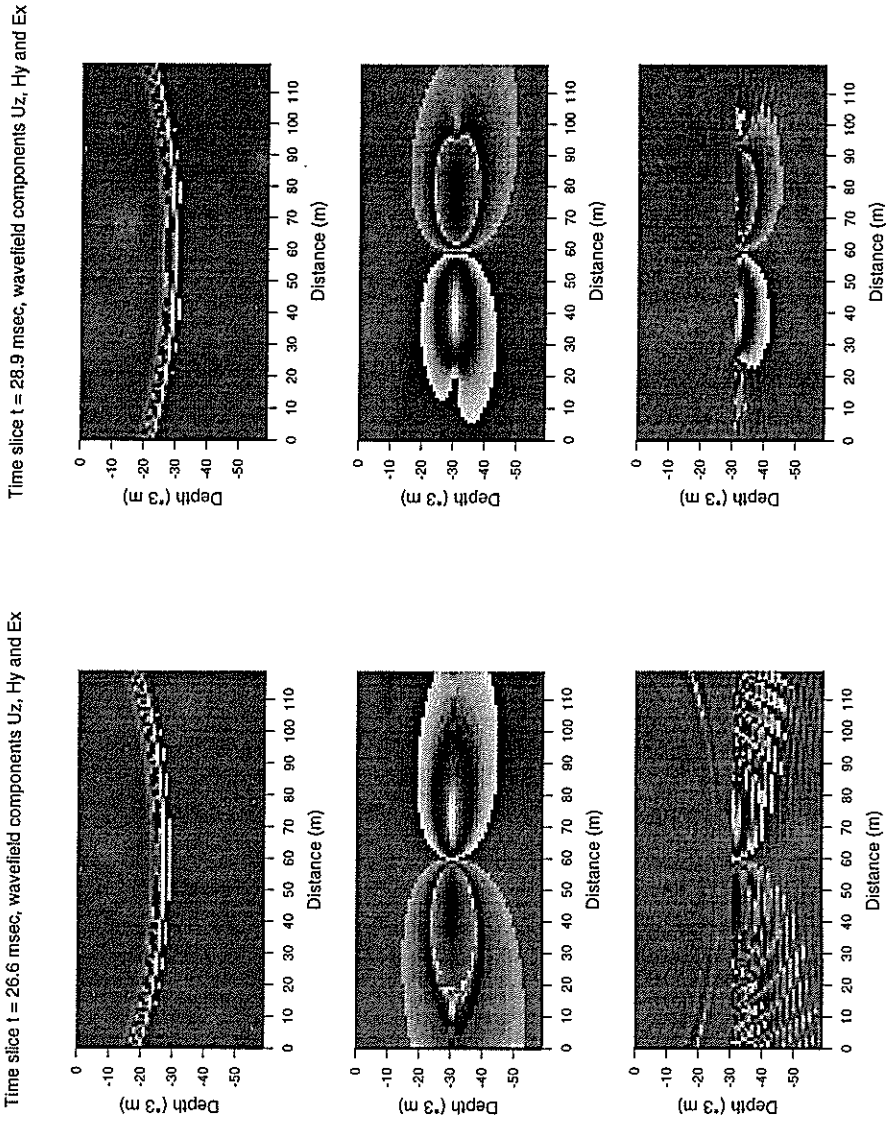

Figure 11: Time slice snapshots calculated at 120 by 60 geophone/receiver positions around an electrical contrast at $t = 26.6$ *msec* and $t = 28.9$ *msec* after explosion. Top snapshot is u_z component of mechanical displacement wavefield, middle snapshot is H_y component of electromagnetic TM mode, bottom snapshot is E_x component of electromagnetic TM mode.

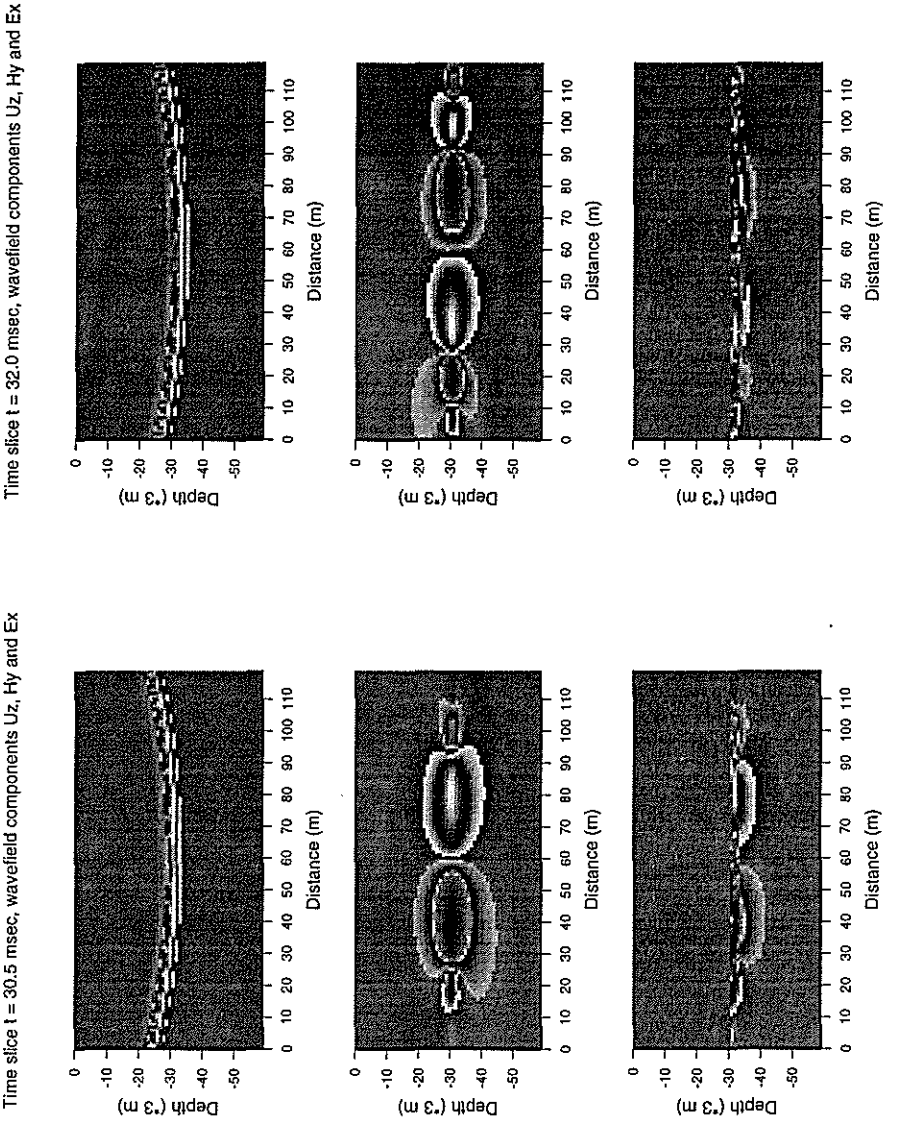

Figure 12: Time slice snapshots calculated at 120 by 60 geophone/receiver positions around an electrical contrast at $t = 30.5$ *msec* and $t = 32.0$ *msec* after explosion. Top snapshot is u_z component of mechanical displacement wavefield, middle snapshot is H_y component of electromagnetic TM mode, bottom snapshot is E_x component of electromagnetic TM mode.

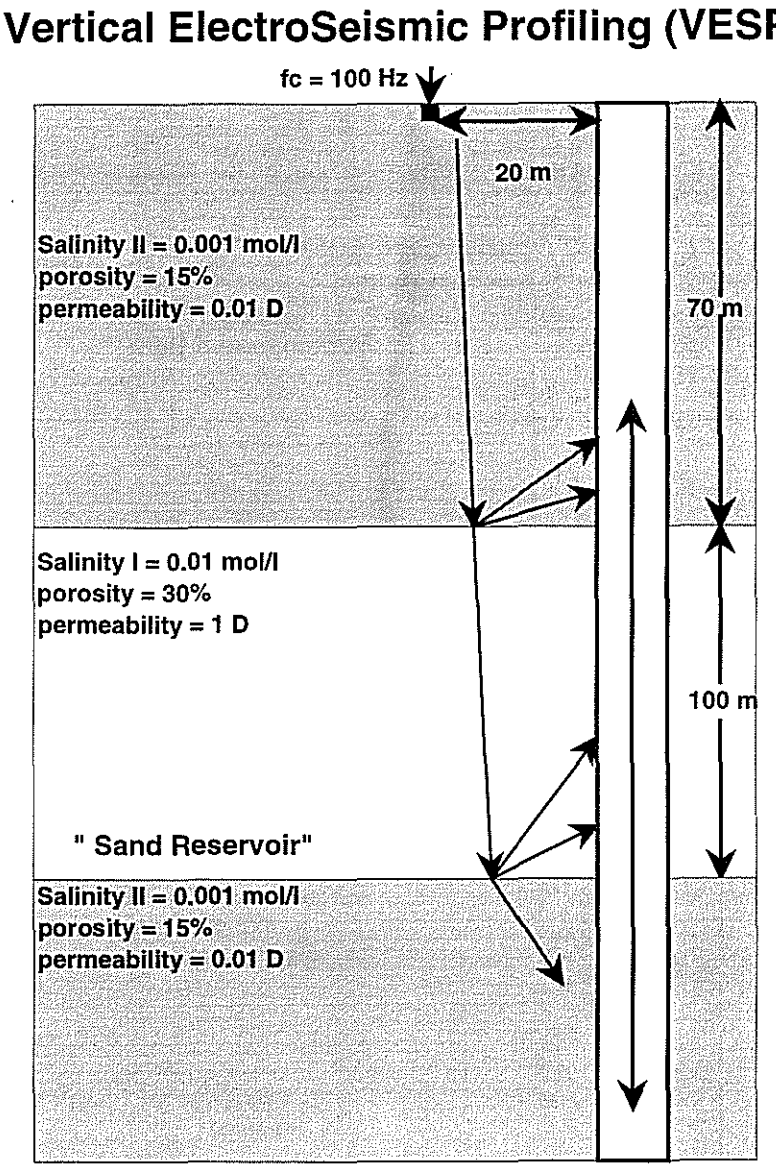

Figure 13: Vertical Electroseismic Profiling medium configuration.

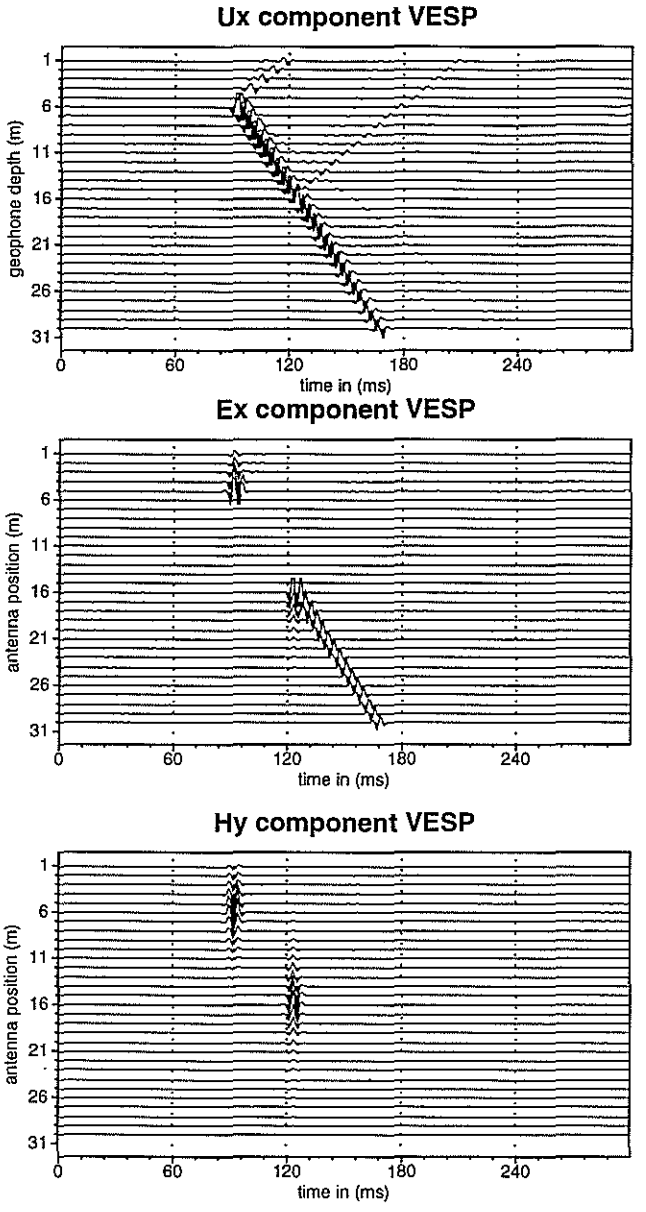

Figure 14: The mechanical displacement component seismogram and the TM mode component electroseismograms calculated for a Vertical Electroseismic Profiling medium configuration.

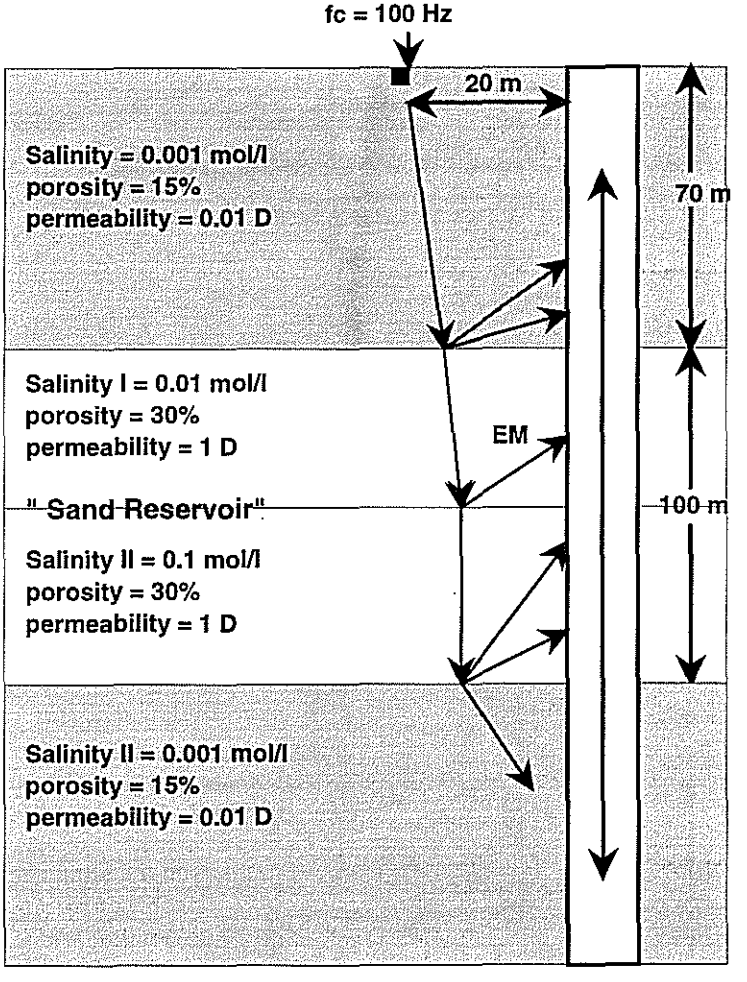

Figure 15: Vertical Electroseismic Profiling medium configuration with additional electrical contrast.

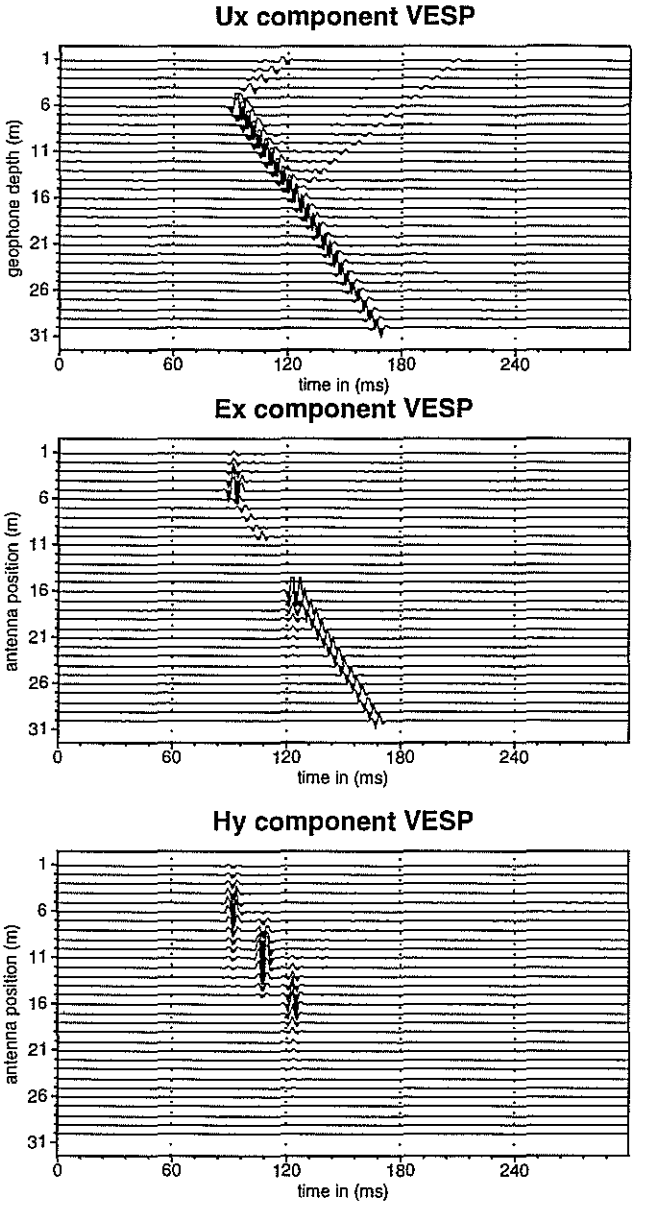

Figure 16: The mechanical displacement component seismogram and the TM mode component electroseismograms calculated for a Vertical Electroseismic Profiling medium configuration with additional electrical contrast.